

On the transient models of the VITAS code: applications in the C5G7-TD pin-resolved benchmark problem

Wei Xiao,¹ Han Yin,¹ Xiaojing Liu,¹ Hui He,¹ and Tengfei Zhang^{1,*}

¹*School of Nuclear Science and Engineering, Shanghai Jiao Tong University, Shanghai 200240, China*

This article describes the transient models of the neutronics code VITAS that are used for solving time-dependent, pin-resolved neutron transport equations using finite elements. VITAS uses the stiffness confinement method (SCM) for the temporal discretization in order to transform the transient equation to a transient eigenvalue problem (TEVP). To solve the pin-resolved TEVP, VITAS incorporates the heterogeneous variational nodal method (VNM). The spatial flux is approximated at each Cartesian node using finite elements in the $x - y$ plane and orthogonal polynomials along the z axis. The angular discretization employs an even-parity integral approach in the nodes and spherical harmonic expansions at the interfaces. To further lower the computational cost, the predictor-corrector quasi-static SCM (PCQ-SCM) is developed. Within the VNM framework, computational models for the adjoint neutron flux and kinetics parameters are presented. The direct-SCM and PCQ-SCM are implemented in VITAS and validated using the 2D and 3D exercises of the OECD/NEA C5G7-TD benchmark. In 2D and 3D problems, the discrepancy between the direct-SCM solver's results and those reported by MPACT and PANDAS-MOC is less than 0.97% and 1.57%, respectively. In addition, numerical studies comparing the PCQ-SCM solver to the direct-SCM solver demonstrate that the PCQ-SCM allows for a substantially larger time-step size, hence reducing the computational cost by a speedup factor of 10 to 100 without compromising numerical accuracy.

Keywords: Stiffness confinement method, quasi-static method, C5G7-TD benchmark, Pin-resolved transient analysis

I. INTRODUCTION

Neutronic calculations play a critical role in analyzing different kinds of nuclear systems[1–3]. Without spatial homogenization and the application of lower order approximations[4], high-fidelity neutron transport methods can accurately predict steady-state and transient behaviors of neutron flux and thermal power during operation or severe accident in nuclear reactors. Solving the transient pin-resolved equation is particularly challenging since the calculation is computationally expensive, and it is difficult to reach a balance between acceptable numerical accuracy and computational costs. The method of characteristics (MOC) and the finite element method (FEM) have shown promise in this area for high-fidelity calculations. In recent years, a number of high-fidelity neutronics codes have been developed. The MOC-based codes MPACT[4], PROTEUS-MOC[5], PANDAS-MOC[6], NECP-X[7, 8] and the FEM-based code Rattlesnake[9] are typical.

In addition, the variational nodal method (VNM) has also shown tremendous promise in solving high-fidelity problems[10]. The VNM is constructed from the functional form of the second-order even-parity transport equation, where odd-parity Lagrange multipliers are applied to enforce the nodal balance[11, 12]. It has been demonstrated that VNM is compatible with a variety of discretization techniques and node geometries. Due to its adaptability and accuracy, the VNM has been successfully implemented in neutronics codes including VARIANT[13], VIOLET[14], VITAS[15], etc. In particular, VITAS is a multi-purpose neutron transport solver that has the high-fidelity modeling capability (namely heterogeneous VNM). Therein, the spatial

flux distribution is approximated with quadratic finite elements and orthogonal polynomials. Within the node, the integral approach for angular discretization is implemented, while spherical harmonics functions are used at the interfaces. These discretization approaches enable VITAS to accomplish refinements in both space and angle.

For the performance of high-fidelity calculations in transient cases, efficient and accurate temporal discretization schemes are essential[16]. The quasi-static approach is the most often adopted temporal discretization scheme among high-fidelity methods. It consists of an improved quasi-static method and a predictor-corrector quasi-static (PCQ) approach[17, 18]. In contrast to direct methods, the computational efficiency of the PCQ method is accomplished by coupling the transport equation and exact point kinetics equation (EPKE) based on the observation that the flux shape varies more slowly with time than the flux amplitude. The shape function is calculated by transport calculation with coarse time-steps, but the amplitude function is determined by EPKE calculation with fine time-steps. Consequently, the high-fidelity transport codes utilizing the PCQ approach can provide time-dependent solutions at an acceptable computational cost.

In the PCQ method, the transient problem is typically transformed into a transient fixed source problem (TFSP) based on the backward difference method (BDM), and is then solved by TFSP solvers. In the absence of an efficient acceleration method, however, the TFSP will converge slowly[5]. The stiffness confinement technique (SCM) is another method that can be utilized for treating the temporal dependence. As opposed to the BDM, the SCM transforms the transient problem into a transient eigenvalue problem (TEVP). The method was originally proposed to alleviate the stiffness in the point kinetics equation by incorporating the dynamic frequencies[19], and subsequently extended to be used in time-dependent dif-

* Corresponding author, zhangtengfei@sjtu.edu.cn

fusion and transport problems[20–22].

Recent studies on the use of the VNM to time-dependent problems have proved its promise. For instance, the VNM with the SCM has been examined in whole-core transport calculations with spatial homogenization[23]. It was proven that the VNM with SCM can leverage a coarse time-step to drastically minimize computing cost. To obtain an accurate flux amplitude, However, the traditional SCM (denoted as the direct-SCM) still requires finer time-steps than the PCQ method. In high-fidelity transient problems, it may impose large computing overhead. To extend the accurate and efficient application of VNM and SCM to high-fidelity transient situations, it is necessary to develop an improved VNM-SCM framework that incorporates the advantages of other temporal discretization techniques, such as the PCQ method.

In this work, the direct-SCM is employed in conjunction with the VITAS code to solve time-dependent high-fidelity transport problems. The PCQ-SCM is proposed and implemented in VITAS to reduce the computational cost, which incorporates the fundamental idea of PCQ, but obtains the flux shape via solving TEVP, which is transformed by SCM. The purpose of the study is to demonstrate the capability of the heterogeneous VNM for solving transient pin-resolved problems. The remainder of the sections are structured as follows: methods for the direct-SCM, heterogeneous VNM and PCQ-SCM, are introduced and derived in Section II. Section III describes the OECD/NEA C5G7-TD benchmark and its associated 2D and 3D exercises. The results obtained using direct-SCM and PCQ-SCM are compared in detail in Section IV. Moreover, comparisons to other codes are given. Section V presents the conclusions and summary.

II. THEORY

In the SCM, the time-dependent transport equation is first transformed to a TEVP by frequency transformation. Then, by solving TEVP using the steady solver iteratively, the necessary quantities for updating frequencies are obtained. In VITAS, the steady solver based on the heterogeneous solver is applied to solving the TEVP. In the following sections, the frequency-transformed equation is derived which yields the form of TEVP. Then, based on the heterogeneous VNM, the nodal functional of the TEVP is presented and discretized to obtain response matrix equations. Next, the flowchart of the essential iteration for updating frequencies in the direct-SCM is presented. Last, the PCQ-SCM is formulated based on the direct-SCM and the EPKE.

A. Frequency-transformed equation

The dynamic frequency of the scalar flux is defined as:

$$\omega_g(\mathbf{r}, t) \equiv \frac{1}{\phi_g(\mathbf{r}, t)} \frac{\partial}{\partial t} \phi_g(\mathbf{r}, t) \quad (1)$$

in which the scalar flux $\phi_g(\mathbf{r}, t)$ of group g is given by:

$$\phi_g(\mathbf{r}, t) = \int d\Omega \psi_g(\mathbf{r}, \Omega, t) \quad (2)$$

where $\psi_g(\mathbf{r}, \Omega, t)$ is the angular flux at position \mathbf{r} in direction Ω . Note that to remove factors of π from these equations, $d\Omega$ is normalized such that $\int d\Omega = 1$. Generally, it is supposed that the dynamic frequency of the angular flux is isotropic such that:

$$\omega_g(\mathbf{r}, t) = \frac{1}{\psi_g(\mathbf{r}, \Omega, t)} \frac{\partial}{\partial t} \psi_g(\mathbf{r}, \Omega, t) \quad (3)$$

Then, the time-variant angular flux can be expressed as:

$$\psi_g(\mathbf{r}, \Omega, t) = \psi_g(\mathbf{r}, \Omega, t_0) e^{\int_{t_0}^t dt' \omega_g(\mathbf{r}, t')} \quad (4)$$

The dynamic frequency can be further decomposed as $\omega_g(\mathbf{r}, t) = \omega_{S,g}(\mathbf{r}, t) + \omega_T(t)$ [21]. The flux amplitude frequency $\omega_T(t)$ represents a global quantity and is dependent only on time; the flux shape frequency $\omega_{S,g}(\mathbf{r}, t)$ is dependent on the space, time and energy. With this approximation, the angular flux can be decomposed using the amplitude term and the shape term as:

$$\psi_g(\mathbf{r}, \Omega, t) = P(t) \hat{\psi}_g(\mathbf{r}, \Omega, t) \quad (5)$$

in which $P(t)$ is the flux amplitude, and $\hat{\psi}_g(\mathbf{r}, \Omega, t_0)$ is the flux shape. The time-variant flux amplitude and flux shape are evaluated as:

$$P(t) = P(t_0) e^{\int_{t_0}^t dt' \omega_T(t')} \quad (6)$$

$$\hat{\psi}_g(\mathbf{r}, \Omega, t) = \hat{\psi}_g(\mathbf{r}, \Omega, t_0) e^{\int_{t_0}^t dt' \omega_{S,g}(\mathbf{r}, t')} \quad (7)$$

To make the decomposition unique[21], a physics-based constraint on the shape frequency is introduced:

$$\sum_{g=1}^G \int_V d\mathbf{r} \nu \Sigma_{f,g}(\mathbf{r}, t) \int d\Omega \hat{\psi}_g(\mathbf{r}, \Omega, t) = P(t_0) \quad (8)$$

where, ν is the number of released neutrons per fission reaction, $\Sigma_{f,g}(\mathbf{r}, t)$ is the macroscopic fission cross-section. The constraint guarantees that the shape frequency affects only the flux shape, not the amplitude. Similarly, the precursor concentration frequency of delayed group i is defined as:

$$\mu_i(\mathbf{r}, t) \equiv \frac{1}{C_i(\mathbf{r}, t)} \frac{\partial}{\partial t} C_i(\mathbf{r}, t) \quad (9)$$

in which $C_i(\mathbf{r}, t)$ is the precursor concentration at position \mathbf{r} , which is supposed to be isotropic commonly. Introducing Eqs. 3 and 9 to the time-dependent transport equation[23] with isotropic-scattering, the frequency-transformed neutron transport equations are obtained:

$$\begin{aligned} & \frac{\omega_T(t) + \omega_{S,g}(\mathbf{r}, t)}{v_g(\mathbf{r})} \psi_g(\mathbf{r}, \Omega, t) + \Omega \cdot \nabla \psi_g(\mathbf{r}, \Omega, t) \\ & + \Sigma_{tg}(\mathbf{r}, t) \psi_g(\mathbf{r}, \Omega, t) \\ & = \Sigma_{sg}(\mathbf{r}, t) \phi_g(\mathbf{r}, t) + q_g(\mathbf{r}, t) \quad g = 1, \dots, G \end{aligned} \quad (10)$$

where $\Sigma_{tg}(\mathbf{r}, t)$ and $\Sigma_{sg}(\mathbf{r}, t)$ are the macroscopic total and scattering cross-sections, respectively. The group source $q_g(\mathbf{r}, t)$ is the contributions from scattering, prompt and delayed neutrons:

$$q_g(\mathbf{r}, t) = \sum_{g' \neq g} \Sigma_{sgg'}(\mathbf{r}, t) \phi_{g'}(\mathbf{r}, t) + \left\{ \begin{array}{l} \chi_g(\mathbf{r}) [1 - \beta(\mathbf{r})] \\ + \sum_{i=1}^I \frac{\chi_{ig}(\mathbf{r}) \beta_i(\mathbf{r}) \lambda_i(\mathbf{r})}{\mu_i(\mathbf{r}, t) + \lambda_i(\mathbf{r})} \end{array} \right\} \times \sum_{g'} \nu \Sigma_{fg'}(\mathbf{r}, t) \phi_{g'}(\mathbf{r}, t) \quad (11)$$

in which $\Sigma_{sgg'}(\mathbf{r}, t)$ is the macroscopic scattering cross-section, $\chi_g(\mathbf{r})$ and $\chi_{ig}(\mathbf{r})$ are fission spectra of prompt and delayed neutrons, $\beta_i(\mathbf{r})$ and $\beta(\mathbf{r})$ are fractions of delayed neutrons, and $\lambda_i(\mathbf{r})$ is the delayed constant of the precursor. The frequency-transformed precursor equations are given as:

$$\mu_i(\mathbf{r}, t) C_i(\mathbf{r}, t) = \beta_i(\mathbf{r}) \sum_{g'} \nu \Sigma_{fg'}(\mathbf{r}, t) \phi_{g'}(\mathbf{r}, t) - \lambda_i(\mathbf{r}) C_i(\mathbf{r}, t) \quad i = 1, \dots, I \quad (12)$$

Introducing the dynamic eigenvalue k_D in Eq. 10 and moving the frequency term to the right-hand-side, the equation can be transformed into an eigenvalue problem (EVP) as:

$$\Omega \cdot \nabla \psi_g(\mathbf{r}, \Omega, t) + \Sigma_{tg}(\mathbf{r}, t) \psi_g(\mathbf{r}, \Omega, t) = \Sigma_{sg}(\mathbf{r}, t) \phi_g(\mathbf{r}, t) + q'_g(\mathbf{r}, t) \quad (13)$$

$$q'_g(\mathbf{r}, t) = \sum_{g' \neq g} \Sigma_{sgg'}(\mathbf{r}, t) \phi_{g'}(\mathbf{r}, t) - \frac{\omega_T(t) + \omega_{Sg}(\mathbf{r}, t)}{v_g(\mathbf{r})} \phi_g(\mathbf{r}, t) + k_D^{-1} \chi'_g(\mathbf{r}, t) \sum_{g'} \nu \Sigma_{fg'}(\mathbf{r}, t) \phi_{g'}(\mathbf{r}, t) \quad (14)$$

where $\chi'_g(\mathbf{r}, t)$ is the dynamic fission spectrum, which is defined as:

$$\chi'_g(\mathbf{r}, t) \equiv \chi_g(\mathbf{r}) [1 - \beta(\mathbf{r})] + \sum_{i=1}^I \frac{\chi_{ig}(\mathbf{r}) \beta_i(\mathbf{r}) \lambda_i(\mathbf{r})}{\mu_i(\mathbf{r}, t) + \lambda_i(\mathbf{r})} \quad (15)$$

After being transformed to an EVP problem, Eq. 13 can be solved with an existing neutron transport solver. The dynamic frequencies resulting in the dominant eigenvalue equal to 1 are the solutions to Eq. 13. Thus, the dynamic frequencies are solved iteratively using power iteration and the secant method to non-linear equations. This non-linear iteration algorithm to frequency-transformed equations is named as the $k - \omega$ iteration[23], which is illustrated in Fig. 1.

B. Variational nodal formulation

In this section, the discretized functional of EVP is derived for the VNM. Last, the corresponding response matrix equations are presented in a multigroup framework.

1. The discretized functional

In the VNM, the even- and odd-parity flux ψ^+ and ψ^- are defined, and the corresponding functional in a node ν can be written with explicit separation of the radial and axial interfaces as[11]:

$$F_\nu[\psi^+, \psi^-] = \int_\nu d\mathbf{r} \left\{ \int d\Omega \left[\Sigma_t'^{-1} (\Omega \cdot \nabla \psi^+)^2 + \Sigma_t' \psi^{+2} \right] - \Sigma_s \phi^2 - 2\phi q' \right\} + 2 \int dz \int_\Gamma d\Gamma \int d\Omega \mathbf{n}_p \cdot \Omega \psi^+ \psi^- + 2 \int_A dA \int d\Omega \left(\mathbf{n}_{z+} \cdot \Omega \psi^+ \psi^-|_{z+} - \mathbf{n}_{z-} \cdot \Omega \psi^+ \psi^-|_{z-} \right) \quad (16)$$

For brevity, \mathbf{r} , Ω and t in the unknowns are suppressed. In the local coordinate, the node is defined in $-\Delta z/2 \leq z \leq \Delta z/2$, the planar area is $A = \Delta x \Delta y$, \mathbf{n}_p is the outward normal to the lateral interfaces extending over the periphery Γ , \mathbf{n}_{z+} and \mathbf{n}_{z-} are the outward normal to the top and bottom axial interfaces, respectively. The functional in the whole problem domain is the superposition of the functional in each nodal volume as $F[\psi^+, \psi^-] = \sum_\nu F_\nu[\psi^+, \psi^-]$.

Within the node, the spatial distribution of the even-parity flux is approximated by:

$$\psi^+(\mathbf{r}, \Omega, t) \approx \mathbf{f}_z^T(z) \otimes \mathbf{g}^T(x, y) \psi(\Omega, t) \quad (17)$$

The scalar flux can be expanded as:

$$\phi(\mathbf{r}, t) = \mathbf{f}_z^T(z) \otimes \mathbf{g}^T(x, y) \phi(t) \quad (18)$$

where the time-dependent scalar flux moments are defined by $\phi(t) = \int d\Omega \psi(\Omega, t)$. $\mathbf{f}_z(z)$ is a vector of orthogonal polynomials defined in the node ν . The polynomials are governed by:

$$\int dz \mathbf{f}_z^T(z) \mathbf{f}_z(z) = \Delta z \mathbf{I} \quad (19)$$

where \mathbf{I} is an identity matrix. $\mathbf{g}(x, y)$ is a vector of continuous finite-element basis functions. The triangular and quadrilateral iso-parametric quadratic finite elements (FE)[11] are employed to map curved interfaces between materials. Fig. 2 shows the FE mesh with 32-elements used to describe a fuel pin cell in this paper.

The odd-parity flux on the axial interface is approximated by:

$$\psi^-(\mathbf{r}, \Omega, t) \approx \mathbf{f}_z^T(\pm \Delta z/2) \mathbf{y}_z^T(\Omega) \otimes \mathbf{h}^T(x, y) \chi_z(t) + \mathbf{f}_{zo}^T(\pm \Delta z/2) \mathbf{y}_{zo}^T(\Omega) \otimes \mathbf{h}^T(x, y) \chi_{zo}(t) \quad (20)$$

in which $\mathbf{h}(x, y)$ is a vector of piecewise constants. $\mathbf{y}_z^T(\Omega)$ and $\mathbf{y}_{zo}^T(\Omega)$ are odd-parity spherical harmonic vectors comprised of both sine and cosine functions[24]. The vectors $\mathbf{y}_z^T(\Omega)$ are low-order P_n approximations, while $\mathbf{y}_{zo}^T(\Omega)$ and $\mathbf{y}_{zo}^T(\Omega)$ contain higher-order terms from $n+2$ to some larger number N . In this paper, we refer to these as approximations.

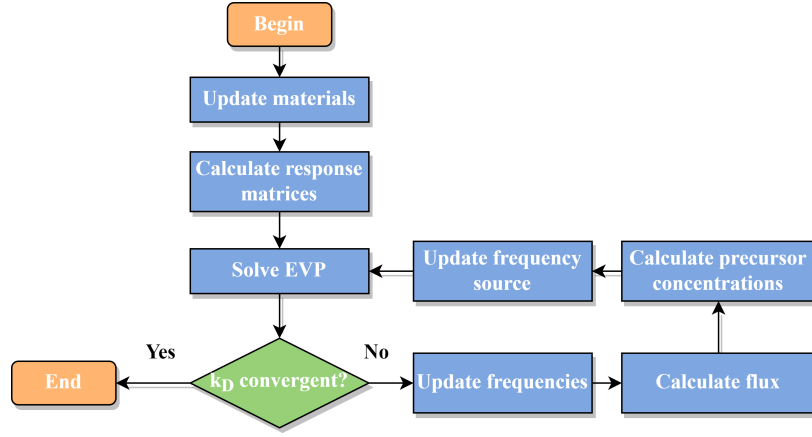


Fig. 1. Flowchart of the $k - \omega$ iteration

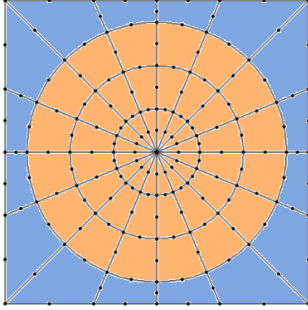


Fig. 2. A finite element mesh for a fuel pin. The orange and blue colors represent the fuel region and the moderator region, respectively

the discretized functional:

$$\begin{aligned}
 F[\psi, \chi_\gamma, \chi_z] = & \int d\Omega \psi^T(\Omega, t) \mathbf{A}(\Omega, t) \psi(\Omega, t) \\
 & - \phi^T(t) \mathbf{I}_z \otimes \mathbf{F}_s(t) \phi(t) - 2\phi(t)^T \mathbf{q}'(t) \\
 & + 2 \sum_\gamma \int d\Omega \psi^T(\Omega, t) \mathbf{E}_\gamma(\Omega) \chi_\gamma(t) \\
 & + 2 \sum_\gamma \int d\Omega \psi^T(\Omega, t) \mathbf{E}_z(\Omega) \chi_z(t) \\
 & + 2 \sum_\gamma \int d\Omega \psi^T(\Omega, t) \mathbf{E}_{\gamma o}(\Omega) \chi_{\gamma o}(t) \\
 & + 2 \sum_\gamma \int d\Omega \psi^T(\Omega, t) \mathbf{E}_{zo}(\Omega) \chi_{zo}(t)
 \end{aligned} \quad (22)$$

$\chi_z(t)$ and $\chi_{zo}(t)$ are the corresponding low- and high-order moments of the odd-parity flux on the axial interfaces.

The odd-parity flux on the lateral interfaces is approximated by:

$$\begin{aligned}
 \psi^-(\mathbf{r}, \Omega, t) = & \mathbf{y}_\gamma^T(\Omega) \otimes \mathbf{f}_\gamma^T(\zeta) \chi_\gamma(t) \\
 & + \mathbf{y}_{\gamma o}^T(\Omega) \otimes \mathbf{f}_{\gamma o}^T(\zeta) \chi_{\gamma o}(t) \quad (21) \\
 & \gamma = x, y \quad \zeta = y, x
 \end{aligned}$$

where $\gamma = 1, 2, 3, 4$ corresponds to the $\gamma = x^-, x^+, y^-, y^+$ lateral interfaces. In VITAS, $\mathbf{f}_\gamma^T(\zeta)$ and $\mathbf{f}_{\gamma o}^T(\zeta)$ are chosen as fourth-order polynomials. Similarly, $\mathbf{y}_\gamma^T(\Omega)$ and $\mathbf{y}_{\gamma o}^T(\Omega)$ are low- and high-order P_n approximations, and $\chi_\gamma(t)$ and $\chi_{\gamma o}(t)$ are the corresponding low- and high-order moments of the odd-parity flux on the lateral interfaces.

Inserting the trial functions of Eqs. 17, 18, 20 and 21 yields

$$\mathbf{q}'(t) = \int d\mathbf{r} \mathbf{f}_z(z) \otimes \mathbf{g}(x, y) \mathbf{q}'(\mathbf{r}, t) \quad (23)$$

in which \mathbf{A} and \mathbf{E} are coefficients matrices. The matrices containing integrals over the spatial trial functions are evaluated numerically using standard FE techniques. The definitions of these matrices are detailed in the previously published research[11, 12]. Requiring the discretized functional Eq. 22 to be stationary with respect to variation in $\psi(\Omega, t)$ yields:

$$\begin{aligned}
 \mathbf{A}(\Omega, t) \psi(\Omega, t) - \mathbf{I}_z \otimes \mathbf{F}_s \phi(t) \\
 = \mathbf{q}'(t) - \mathbf{E}_l(\Omega) \chi_l(t) - \mathbf{E}_o(\Omega) \chi_o(t) \quad (24)
 \end{aligned}$$

Note that the terms in Eq. 24 is re-grouped by low-order (with subscript l) and high-order (with subscript o) terms.

2. Nodal response matrix equations

The odd-parity moments χ_l and χ_o are defined to be continuous across interfaces. Also, requiring Eq. 22 to be stationary with respect to variations in χ_l and χ_o yields that the

even-parity flux is continuous across the interfaces:

$$\varphi_l(t) = \Lambda^{-1} \int d\Omega \mathbf{E}_l^T(\Omega) \psi(\Omega, t) \quad (25)$$

With integration over the angle and matrix operations[11] to Eq. 24, the scalar flux can be determined in terms of the response matrix equations given as:

$$\phi(t) = \mathbf{V}(t) \mathbf{q}'(t) - \mathbf{C}(t) [\mathbf{j}^+(t) - \mathbf{j}^-(t)] \quad (26)$$

The coefficients matrices can be also found in [11, 12]. \mathbf{j}^+ and \mathbf{j}^- correspond to the interfacial expansion moments of outgoing and incoming neutron currents, respectively. They are defined as:

$$\mathbf{j}^\pm(t) = \frac{1}{4} \varphi_l(t) \pm \frac{1}{2} \chi_l(t) \quad (27)$$

The outgoing currents moments \mathbf{j}^+ satisfy:

$$\mathbf{j}^+(t) = \mathbf{B}(t) \mathbf{q}'(t) + \mathbf{R}(t) \mathbf{j}^-(t) \quad (28)$$

To sum up, the flowchart of the iteration in the VNM is illustrated in Fig. 3.

C. Direct-SCM in VNM

The application of high-order iso-parametric FEs incurs significant computational costs and the memory usage. To alleviate this burden, the element-wise flux values are stored in the code rather than vertex-wise values generally adopted in the FEM. The element-wise average scalar flux is defined as:

$$\bar{\phi}(t) = \Xi^{-1} \int dxdy \mathbf{h}(x, y) \mathbf{g}^T(x, y) \phi_0(t) \quad (29)$$

where $\phi_0(t)$ is the segment of $\phi(t)$ corresponding to the components of the vector of orthogonal polynomials $\mathbf{f}_z(z)$ of order 0, and Ξ is a diagonal matrix composed of the FE areas. $\mathbf{h}(x, y)$ is a vector of piecewise functions, which are equal to one on the domain of the corresponding FE and zero elsewhere. By averaging over each FE, the number of stored values is significantly reduced. Correspondingly, the flux shape frequency and precursor concentration are also defined as the element-wise quantity. For brevity, the subscription ν and k denote the average quantity in element k of node ν in Section II C. For example, $\phi_{\nu k, g}(t)$ is the element-wise average scalar flux of group g in element k of node ν .

The calculation procedure of the direct-SCM within the framework of the VNM is given in Fig. 4. In the $k - \omega$ iteration, the secant method[21] can be applied to update the amplitude frequency. The update formula of the amplitude frequency based on the secant method is shown as:

$$\begin{aligned} \omega_T^{(m+1)}(t_n) &= \omega_T^{(m)}(t_n) \\ &+ \left[\omega_T^{(m-1)}(t_n) - \omega_T^{(m)}(t_n) \right] \frac{1 - k_D^{(m)}}{k_D^{(m-1)} - k_D^{(m)}} \end{aligned} \quad (30)$$

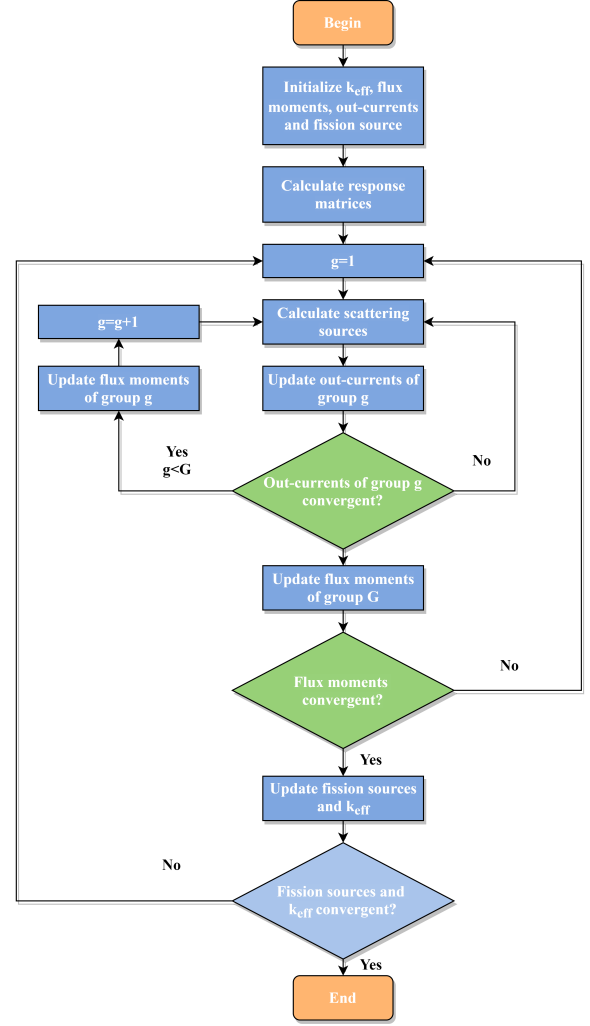


Fig. 3. Flowchart of the iteration in the VNM

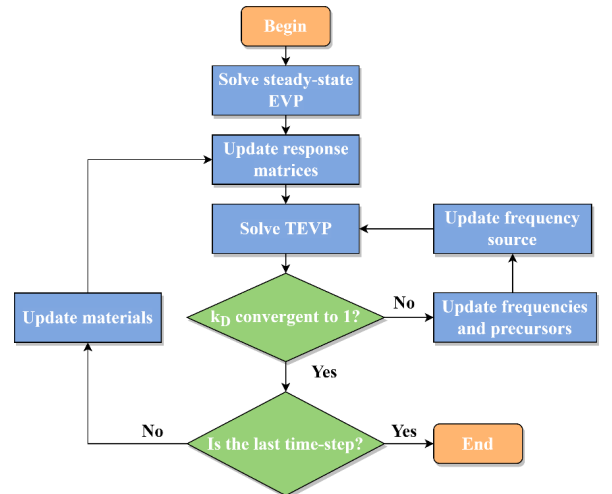


Fig. 4. Flowchart of the transient calculations with direct-SCM on VNM

where m denotes the iteration step of the $k - \omega$ iteration. The

normalized element-wise average scalar flux $\hat{\phi}_{\nu k, g}(t_n)$ are obtained by:

$$\hat{\phi}_{\nu k, g}(t_n) = \tilde{\phi}_{\nu k, g}(t_n) \times \frac{P(t_{n-1})}{\sum_{\nu} \sum_k \sum_{g=1}^G \nu \Sigma_{\nu k, fg}(t_n) A_{\nu k} \tilde{\phi}_{\nu k, g}(t_n)} \quad (31)$$

in which $A_{\nu k}$ is the element's area, $\tilde{\phi}_{\nu k, g}(t_n)$ is the element-wise average scalar flux obtained from the EVP solver directly before the normalization. This normalization enforces the total power contributed by the normalized flux to equal the power of the previous time-step. Therefore, the shape frequency obtained from the normalized flux is independent of the flux amplitude. Additionally, it is supposed that the shape frequency is homogeneous within the element. Thus, based on the isotropic and homogeneous approximation, the element-wise shape frequency is calculated as:

$$\omega_{\nu k, S, g}(t_n) = \frac{1}{\Delta t_n} \ln \left[\frac{\hat{\phi}_{\nu k, g}(t_n)}{\hat{\phi}_{\nu k, g}(t_{n-1})} \right] \quad (32)$$

where $\Delta t_n = t_n - t_{n-1}$, and $\omega_{\nu k, S, g}(t_n)$ is the element-wise shape frequency within $[t_{n-1}, t_n]$.

It is supposed that the amplitude frequency varies linearly within $[t_{n-1}, t_n]$:

$$\omega_T(t) = \omega_T(t_{n-1}) + \frac{\omega_T(t_n) - \omega_T(t_{n-1})}{\Delta t} (t - t_{n-1}) \quad (33)$$

Then, according to Eq. 5, the actual element-wise average scalar flux is:

$$\begin{aligned} \phi_{\nu k, g}(t_n) &= \phi_{\nu k, g}(t_{n-1}) e^{\frac{\omega_T(t_n) + \omega_T(t_{n-1})}{2} \Delta t_n + \omega_{\nu k, S, g}(t_n) \Delta t_n} \\ &= \hat{\phi}_{\nu k, g}(t_n) e^{\frac{\omega_T(t_n) + \omega_T(t_{n-1})}{2} \Delta t_n} \end{aligned} \quad (34)$$

The first-order analytical precursor integration method is implemented to calculate the precursor concentration, where the fission source is supposed to vary linearly across the time-step $[t_{n-1}, t_n]$. The analytical solution to the element-wise precursor concentration is then expressed as:

$$\begin{aligned} C_{\nu k, i}(t_n) &= C_{\nu k, i}(t_{n-1}) e^{-\lambda_{\nu k, i} \Delta t_n} \\ &+ \beta_{\nu k, i} e^{-\lambda_{\nu k, i} \Delta t_n} \int_{t_{n-1}}^{t_n} Q_{\nu k}(t) e^{\lambda_{\nu k, i} t} dt \end{aligned} \quad (35)$$

in which the element-wise fission source $Q_{\nu k}(t)$ is expressed as:

$$Q_{\nu k}(t) = Q_{\nu k}(t_{n-1}) + \frac{Q_{\nu k}(t_n) - Q_{\nu k}(t_{n-1})}{\Delta t_n} (t - t_{n-1}) \quad (36)$$

$$Q_{\nu k}(t_n) = \kappa \Sigma_{\nu k, fg}(t_n) \phi_{\nu k, g}(t_n) \quad (37)$$

The update formula of the element-wise precursor frequency is given as:

$$\mu_{\nu k, i}(t_n) = \begin{cases} \beta_{\nu k, i} \frac{Q_{\nu k}(t_n)}{C_{\nu k, i}(t_n)} - \lambda_{\nu k, i} & C_{\nu k, i}(t_n) \neq 0 \\ 0 & C_{\nu k, i}(t_n) = 0 \end{cases} \quad (38)$$

D. PCQ-SCM in VNM

To reduce the computational cost without a significant loss of the accuracy, the PCQ-SCM is proposed. The main idea of the PCQ-SCM is to firstly solve TEVP with a coarse time-step to obtain the predicted neutron flux. Then, by determining kinetics parameters (KPs) with the predicted flux, the EPKE is solved with a fine time-step to obtain the amplitude function. The time-steps specifications are illustrated in Fig. 5. The error of the neutron flux resulting from the coarse time-step is then corrected with the amplitude function.

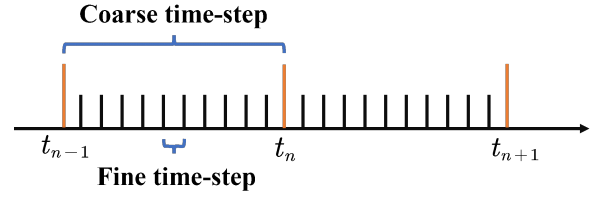


Fig. 5. Illustration of the coarse and fine time-steps in the PCQ-SCM

In the following sections, the PCQ-SCM is derived from the solution to the adjoint equation with VNM. Then, the approach for evaluating the reactivity and kinetics parameters (KPs) with the VNM-based adjoint flux is discussed.

1. Adjoint solution in VNM

The solution to the adjoint steady transport equation, i.e., the adjoint neutron flux, is adopted as a weighting function in the perturbation problems. For example, the exact point kinetics equation (EPKE) is derived from the first-order perturbation theory with the adjoint flux as the weighting function[25, 26]. To implement the PCQ method in the transient calculation, the VNM based adjoint flux should be used as the weighting function.

The VNM transforms the original transport equation to a second-order even-parity equation. Since the leakage operator in the second-order even-parity equation is self-adjoint[27], the adjoint calculation is simplified significantly. The forward and adjoint response matrix equations differ only in the source term. As a result, forward and adjoint calculations can be performed using the same within-group algorithms and response matrices shown in Fig. 3. The adjoint source term can be constructed by switching the group number of the scattering and fission cross-sections.

In the following derivations, an asterisk denotes the solution to the adjoint equation. The adjoint response matrix equations at the initial condition are given as:

$$\phi^*(t_0) = V(t_0) \mathbf{q}^*(t_0) - C(t_0) [\mathbf{j}^{*+}(t_0) - \mathbf{j}^{*-}(t_0)] \quad (39)$$

$$\mathbf{j}^{*+}(t_0) = B(t_0) \mathbf{q}^*(t_0) + R(t_0) \mathbf{j}^{*-}(t_0) \quad (40)$$

where the response matrices are identical to those in Eqs. 26

and 28. The vector of the initial adjoint source $\mathbf{q}^*(t_0)$ is defined as:

$$\mathbf{q}^*(t_0) = \int dr \mathbf{f}_z(z) \otimes \mathbf{g}(x, y) \mathbf{q}^*(\mathbf{r}, t_0) \quad (41)$$

$$q_g^*(\mathbf{r}, t_0) = \sum_{g' \neq g} \Sigma_{sg'g}(\mathbf{r}, t_0) \phi_{g'}^*(\mathbf{r}, t_0) + k_{\text{eff}}^{-1} \nu \Sigma_{fg}(\mathbf{r}, t_0) \sum_{g'} \chi_{g'}^*(\mathbf{r}, t_0) \phi_{g'}^*(\mathbf{r}, t_0) \quad (42)$$

$$\chi_g^*(\mathbf{r}, t_0) = \chi_g(\mathbf{r}) [1 - \beta(\mathbf{r})] + \sum_{i=1}^I \chi_{ig}(\mathbf{r}) \beta_i(\mathbf{r}) \quad (43)$$

Note that the eigenvalue k_{eff} in the adjoint equation should be identical to that in the forward equation.

2. Exact point kinetics equation

The EPKE is derived from the transient transport equation[28]. Similarly, the neutron flux is factorized into the shape function and the amplitude function as:

$$\psi_g(\mathbf{r}, \boldsymbol{\Omega}, t) = T(t) \tilde{\psi}_g(\mathbf{r}, \boldsymbol{\Omega}, t) \quad (44)$$

where $T(t)$ is the amplitude function, and $\tilde{\psi}_g(\mathbf{r}, \boldsymbol{\Omega}, t)$ is the shape function. Similarly, to make the decomposition unique, the constraint is introduced as:

$$\sum_{g=1}^G \int_V dr \int d\boldsymbol{\Omega} \psi_g^*(\mathbf{r}, \boldsymbol{\Omega}, t_0) \frac{1}{v_g(\mathbf{r})} \tilde{\psi}_g(\mathbf{r}, \boldsymbol{\Omega}, t) = T(t_0) \quad (45)$$

where $\psi_g^*(\mathbf{r}, \boldsymbol{\Omega}, t_0)$ is the adjoint angular flux at the steady-state. It indicates the integral of the shape function with the initial adjoint flux is held constant over time. By inserting Eq. 44 into Eqs. 10 and 12, and multiplying the adjoint flux on both sides, then integrating over all variable, the EPKE is obtained as follows:

$$\frac{d}{dt} T(t) = \frac{\rho(t) - \bar{\beta}(t)}{\Lambda(t)} T(t) + \sum_{i=1}^I \bar{\lambda}_i(t) \zeta_i(t) \quad (46)$$

$$\frac{d}{dt} \zeta_i(t) = \frac{\bar{\beta}_i(t)}{\Lambda(t)} T(t) - \bar{\lambda}_i(t) \zeta_i(t) \quad (47)$$

where $\rho(t)$ is the reactivity, $\bar{\beta}(t)$ and $\bar{\beta}_i(t)$ are effective fractions of delayed neutrons, $\bar{\lambda}_i(t)$ is the effective decay constant, $\Lambda(t)$ is the prompt neutron lifetime, and $\zeta_i(t)$ is the reduced precursor concentration. The detailed formulation of EPKE is available in [17]. Eqs. 46 and 47 can be solved by ordinary differential equation solvers. In VITAS, the ordinary differential equation is developed based on the SCM for EPKE[19].

As shown in Section II B, the even-parity integral method implemented in VITAS only leads to a solution of the scalar flux. Reconstructing the angular flux requires the extra storage of temporary matrices about the discretized operators[11] and extra algebraic operations of these matrices to the scalar flux. Besides, storing the angular flux also increases memory usage significantly. Therefore, the scalar flux is employed as the weighting function to calculate KPs in VITAS. Note that the reactivity is not included in the KPs in this section. The details of KPs calculated with the scalar flux $\tilde{\phi}$ and ϕ^\dagger are listed as follows:

$$F(t) = \sum_{g=1}^G \int dr \left\{ \times \sum_{g'}^G \frac{\chi_g(\mathbf{r})}{k_{\text{eff}}} \phi_g^*(\mathbf{r}, t_0) \tilde{\phi}_{g'}(\mathbf{r}, t) \right\} = \sum_{g=1}^G \sum_{\nu} \sum_k \left\{ \times \sum_{g'}^G \frac{\chi_{\nu k, g}}{k_{\text{eff}}} A_{\nu k} \phi_{\nu k, g}^*(t_0) \tilde{\phi}_{\nu k, g'}(t) \right\} \quad (48)$$

$$\bar{\beta}_i(t) = \frac{\sum_{g=1}^G \int dr \left\{ \times \sum_{g'}^G \frac{\chi_{ig}(\mathbf{r})}{k_{\text{eff}}} \phi_g^*(\mathbf{r}, t_0) \beta_i(\mathbf{r}) \tilde{\phi}_{g'}(\mathbf{r}, t) \right\}}{F(t)} = \frac{\sum_{g=1}^G \sum_{\nu} \sum_k \left\{ \times \sum_{g'}^G \frac{\chi_{\nu k, ig}}{k_{\text{eff}}} A_{\nu k} \phi_{\nu k, g}^*(t_0) \beta_{\nu k, i} \tilde{\phi}_{\nu k, g'}(t) \right\}}{F(t)} \quad (49)$$

$$\Lambda(t) = \frac{\sum_{g=1}^G \int dr \frac{\phi_g^*(\mathbf{r}, t_0) \tilde{\phi}_g(\mathbf{r}, t)}{v_g(\mathbf{r}, t)}}{F(t)} = \frac{T(t_0)}{F(t)} \quad (50)$$

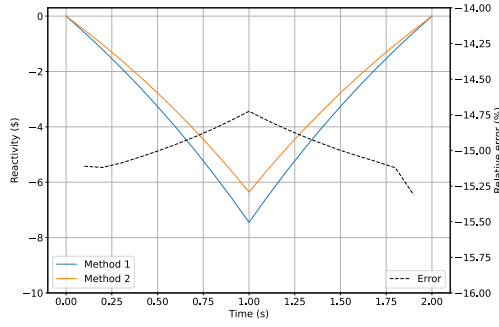
$$\bar{\lambda}_i(t) = \frac{\sum_{g=1}^G \int dr \phi_g^*(\mathbf{r}, t_0) \chi_{ig}(\mathbf{r}) \lambda_i(\mathbf{r}) C_i(\mathbf{r}, t)}{\sum_{g=1}^G \int dr \phi_g^*(\mathbf{r}, t_0) \chi_{ig}(\mathbf{r}) C_i(\mathbf{r}, t)} = \frac{\sum_{g=1}^G \sum_{\nu} \sum_k A_{\nu k} \phi_{\nu k, g}^*(t_0) \chi_{\nu k, ig} \lambda_{\nu k, i} C_{\nu k, i}(t)}{\sum_{g=1}^G \sum_{\nu} \sum_k A_{\nu k} \phi_{\nu k, g}^*(t_0) \chi_{\nu k, ig} C_{\nu k, i}(t)} \quad (51)$$

The related research shows that the KPs calculated with the scalar flux agree well with those calculated with the angular flux[5]. However, using the scalar flux as the weighting function can result in significant deviations in the reactivity[5, 29]. For example, in the moderation density reduction problems of the C5G7-TD benchmark, the scalar flux weighting function underestimates the reactivity by up to 15.6%[5]. The different reactivities resulting from the scalar flux are mainly due to that the leakage operator $\boldsymbol{\Omega} \cdot \nabla$ is highly anisotropic. Therefore, adopting the isotropic approximation to evaluate the perturbation of the leakage operator can cause significant deviation to the reactivity. To obtain an accurate reactivity for the EPKE calculation, the reactivity is evaluated[30] as:

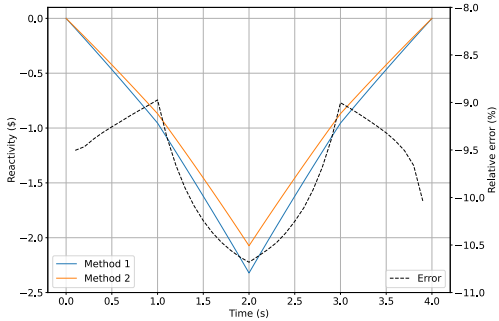
$$\rho(t) = \frac{k_{\text{eff}}(t) - 1}{k_{\text{eff}}(t)} \quad (52)$$

where $k_{\text{eff}}(t)$ is the dynamic eigenvalue, which is defined as the eigenvalue to Eq. 13 with setting frequencies μ and ω to

zeros. Since $k_{\text{eff}}(t)$ is obtained by solving transport EVP, Eq. 52 is equivalent to calculating the reactivity with the angular flux. It eliminates the necessity to reconstructing and storing the angular flux. Additionally, solving for the dynamic eigenvalue does not increase computational cost due to that the SCM requires solving EVPs iteratively shown in Fig. 1. Denoting reactivity evaluation using Eq. 52 as Method 1 and using the weight of scalar flux as Method 2, the comparison of two methods is shown in Fig. 6. The results indicate that the reactivity evaluation using scalar flux underestimates the reactivity by an error of -15.0% and -10.0% in TD3-4 and TD5-1 of C5G7-TD problem respectively, which is consistent with the results reported by [5].



(a) TD3-4



(b) TD5-1

Fig. 6. Reactivity evaluation using different methods in C5G7-TD problems

3. Overall PCQ-SCM scheme

In the PCQ-SCM solver of VITAS, the initial adjoint scalar flux $\phi_g^*(\mathbf{r}, t_0)$ and forward scalar flux $\phi_g(\mathbf{r}, t_0)$ are obtained by solving initial EVPs. The initial amplitude function $T(t_0)$ is determined with $P(t_0)$. Then, in each coarse time-step $[t_{n-1}, t_n]$, the TEVP and the EPKE are solved in the following steps:

1. Solve the predicted scalar flux $\phi_{p,g}(\mathbf{r}, t_n)$, flux amplitude $P_p(t_n)$, and precursor concentrations $C_{p,i}(\mathbf{r}, t)$

using the TEVP in Eq. 13 with $k - \omega$ iteration at t_n . In the first iteration-step, the frequencies μ and ω are set to zero. Then, the eigenvalue obtained in the first iteration-step is the dynamic eigenvalue $k_{\text{eff}}(t_n)$ required in Eq. 52.

2. Determine the reactivity $\rho(t_n)$ with Eq. 52.
3. Calculate the predicted shape function $\tilde{\phi}_{p,g}(\mathbf{r}, t_n)$ with the constraint in Eq. 45 as:

$$\tilde{\phi}_{p,g}(\mathbf{r}, t_n) = \phi_{p,g}(\mathbf{r}, t_n) \times \frac{T(t_0)}{\sum_{g=1}^G \int_V d\mathbf{r} \int d\Omega \phi_g^*(\mathbf{r}, t_0) \frac{1}{v_g(\mathbf{r})} \phi_{p,g}(\mathbf{r}, t_n)} \quad (53)$$

4. Calculate the KPs at t_n with Eqs. 48-51, and solve EPKE to obtain the amplitude function $T(t_n)$ at the fine time-step using the interpolated KPs from the values at t_{n-1} and t_n .

5. Determine the corrected flux amplitude $P_c(t_n)$ and scalar flux $\phi_{c,g}(\mathbf{r}, t_n)$ as follows:

$$P_c(t_n) = \frac{T(t_n) P(t_0)}{T(t_0)} \quad (54)$$

$$\begin{aligned} \phi_{c,g}(\mathbf{r}, t_n) &= \frac{P_c(t_n)}{P_p(t_n)} \phi_{p,g}(\mathbf{r}, t_n) \\ &= P_c(t_n) \hat{\phi}_{p,g}(\mathbf{r}, t_n) \end{aligned} \quad (55)$$

6. Re-calculate the precursor concentrations with the corrected scalar flux by Eq. 35.

Then, iterate through Step 1 to Step 6 in the next coarse time-step until the end of the transient event. The overall flowchart of the PCQ-SCM is shown in Fig. 7.

Additionally, in the PCQ-SCM solver, the amplitude frequency ω_T is approximated as a constant in $[t_{n-1}, t_n]$ to improve the numerical stability in the case with a large time-step. Though the linear approximation adopted in Eq. 33 shows higher accuracy to the constant approximation, the amplitude is corrected with the solution of the EPKE. Therefore, the constant approximation can provide higher stability in large time-step cases without affecting the numerical accuracy. In the PCQ-SCM solver, Eq. 34 is replaced by:

$$\begin{aligned} \phi_{\nu k,g}(t_n) &= \phi_{\nu k,g}(t_{n-1}) e^{\omega_T(t_n) \Delta t_n + \omega_{\nu k,g}(t_n) \Delta t_n} \\ &= \hat{\phi}_{\nu k,g}(t_n) e^{\omega_T(t_n) \Delta t_n} \end{aligned} \quad (56)$$

III. C5G7-TD BENCHMARK PROBLEM

The C5G7-TD transient benchmark is derived from the C5G7 benchmark model[31, 32]. It includes both 2D and 3D models that are used to verify the transient capability for modeling a heterogeneous light water reactor without thermal feedback. In the following sections, the geometry, material and transient exercises in the C5G7-TD are described.

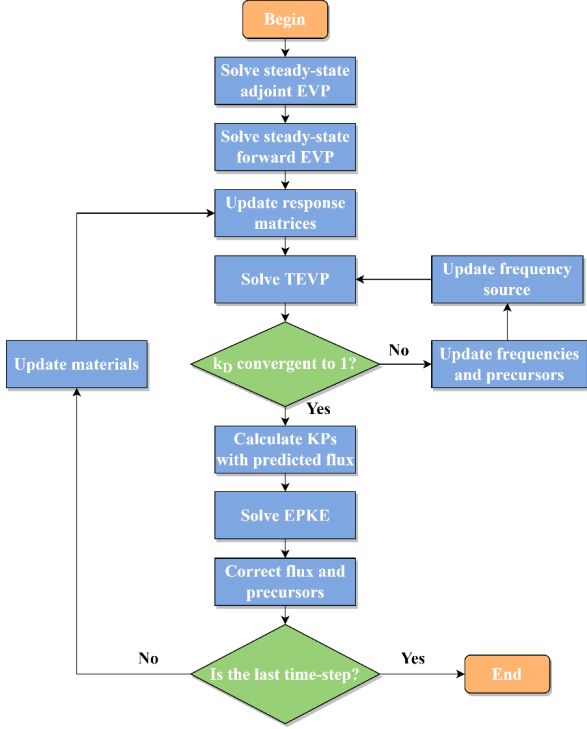


Fig. 7. Flowchart of the transient calculations with PCQ-SCM on VNM

A. Geometry description

The benchmark problem simulates a light water reactor with 8 uranium oxide (UO₂) assemblies, 8 mixed oxide (MOX) assemblies, surrounded by the water reflector. The model is simplified into a quarter core using the reflective boundary on the north and west boundaries and the vacuum boundary on the south and east boundaries, as shown in Fig. 8-a. The four assemblies are numbered 1-4 respectively. The size of the 2D model is 64.26 cm × 64.26 cm. The 3D model has the same planar layout as the 2D model, but in the axial direction, two identical water reflectors are added above and below the active region of the core as shown in Fig. 8-a. The height of the 3D configuration is 171.36 cm while that of the active region is 128.52 cm.

The UO₂ assembly and MOX assembly have identical geometry configurations, but different fuel pin compositions. Their sizes are 21.42 cm × 21.42 cm with a 17 × 17 pin layout. Each assembly consists of 289 pin cells, including 264 fuel pins, 24 guide tubes, and 1 fission chamber as shown in Fig. 8-b. The UO₂ assembly contains one type of fuel pin, while the MOX assembly contains three types of fuel pins with enrichment of 4.3%, 7.0% and 8.7%, respectively.

Each pin cell has a pitch of 1.26 cm and is simplified as two zones as shown in Fig. 8-c. Zone 1 is the circular area with the radius of 0.54 cm. It is filled with fuel, control rod or fission chamber. Zone 2 is located outside of the circular zone and filled with moderator.

B. Material description

The C5G7-TD benchmark adopts multigroup macroscopic cross-sections and kinetics parameters (KPs) for eight materials: UO₂ fuel, 7.0% MOX fuel, 4.3% MOX fuel, 8.7% MOX fuel, guide tube, fission chamber, moderator and control rod[32]. The cross-sections are provided in a 7-group structure including transport-corrected total cross-sections Σ_{tg} , absorption cross-sections Σ_{ag} , fission cross-sections Σ_{fg} , fission spectra χ_g , fission neutron yields ν and scattering cross-sections $\Sigma_{sgg'}$. The KPs are provide in an 8-delayed-group structure including neutron velocities v_g , delayed neutron fission spectra χ_{ig} , delayed neutron fractions β_i and decay constants λ_i .

For the 3D control rod movement problems, such as TD4 problems, to reduce the rod cusping effects, the effective volume fraction proposed by[6] is applied to homogenize the cross-sections of the guide tube and control rod in the partially rodded node. The effective volume fraction (y) of the rod is a polynomial function of the original volume fraction (x), which is the ratio of the inserted rod length to the node height. The polynomial function is given as:

$$y = 0.3867848x + 0.1707878x^2 + 0.9887881x^3 - 5.9535775x^4 + 25.1805898x^5 - 63.1841252x^6 + 98.3898802x^7 - 92.4982596x^8 + 48.0373368x^9 - 10.5182051x^{10} \quad (57)$$

Fig. 9 shows the relations between the original and effective volume fraction with Eq. 57 and linear assumption, respectively.

C. Transient description

The C5G7-TD benchmark problem consists of six exercises labelled TD0-TD5. Each exercise includes a number of cases that simulate the movement of control rod banks or the change in moderator density. To model the control rod movements, the control rods in an assembly are referred to as a rod bank. Control rods in the same bank are simultaneously inserted or withdrawn.

As illustrated in Table 1, TD0, TD1, and TD2 are 2D exercises that require adjusting different control rod banks in a variety of ways. TD0 contains 5 test problems. In TD0, control rods are abruptly inserted into the active region (10% of the core height) at the initial time and remain there for 1 s. Then, control rods are partially extracted (5% of the core height) and stay for 1 s. At the end of 2 s, the control rods are completely withdrawn from the active region.

TD1 and TD2 each contain 5 and 3 test problems. In TD1 and TD2, control rods move linearly at a constant speed. From the starting point at $t=0$ s, control rods are inserted to the maximum depth at $t=1$ s and then returned to the starting point at $t=2$ s. The maximum inserted depth for TD1 and TD2 is 1% and 10% of the core height, respectively. In the 2D model, the control rod movement is simulated as the linear

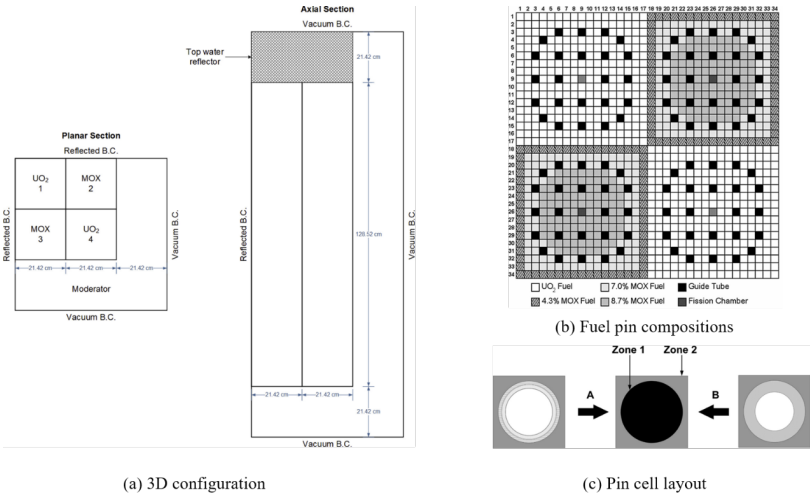


Fig. 8. Geometry and composition of C5G7-TD benchmark

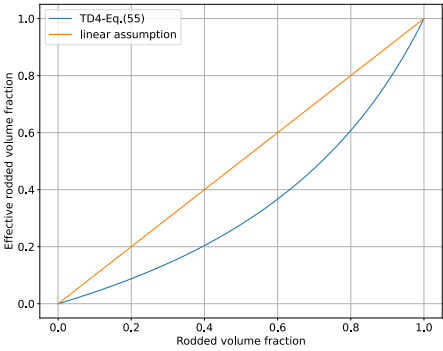


Fig. 9. Relation between original and effective rodded volume fraction

substitution of the moderator-filled guide tube material with the control rod material in Zone 1 of the specified pin cells.

TABLE 1. Scenarios of control rods movement defined in TD0, TD1 and TD2

| Test problem | TD0 | TD1 | TD2 |
|--------------|-----------------|-----------------|--------|
| 1 | Bank 1 | Bank 1 | Bank 1 |
| 2 | Bank 3 | Bank 3 | Bank 3 |
| 3 | Bank 4 | Bank 4 | N/A |
| 4 | Bank 1, 3 and 4 | Bank 1, 3 and 4 | N/A |
| 5 | Bank 1-4 | Bank 1-4 | N/A |

TD3 is a 2D exercise simulating the reactivity insertion caused by the moderator density change in the reactor core. It has 4 test problems. During the first second, the moderator density in all assemblies declines simultaneously and at the same rate from the nominal value to the minimal value. After $t=1$ s, the density increases to the nominal value within the following second. These four test problems differ in the ratio of the minimum to the nominal

value as shown in 10.

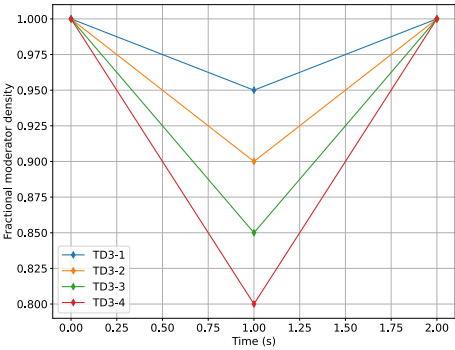


Fig. 10. Fractional moderator density change in TD3 exercise

TD4 is a 3D exercise that simulates the process of insertion and withdrawal of control rods. It contains 5 problems. In the initial phase, all control rods are placed in the top water reflector, outside the active region. These five problems involve continual insertion and removal of various combinations of control rod banks. Fig. 11 depicts the control rod banks and the relative insertion length to the active core length for each problem.

Similar to TD3, TD5 is a 3D transient event initiated by the moderator density change with all control rods fully withdrawal. The moderator density in the same assembly changes simultaneously. For each of the four test problems, the density of the moderator varies in each of the four assemblies as shown in 12.

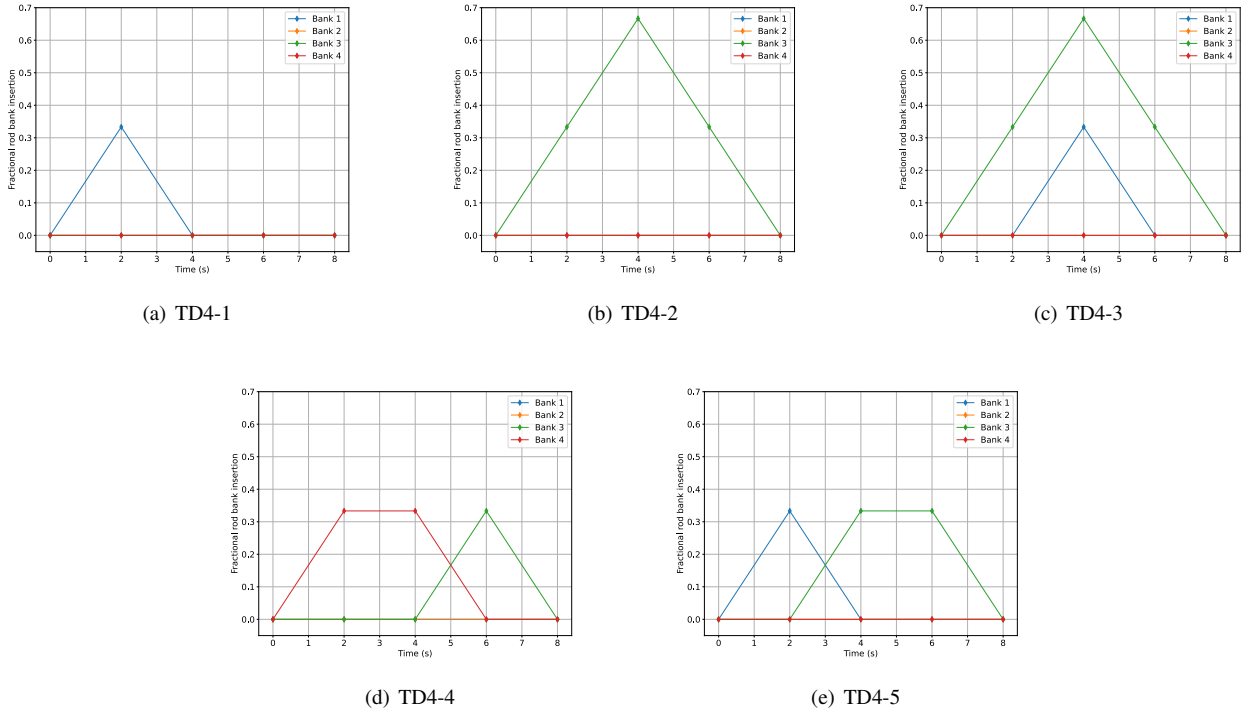


Fig. 11. Relative depth of control bank movement in TD4 exercise

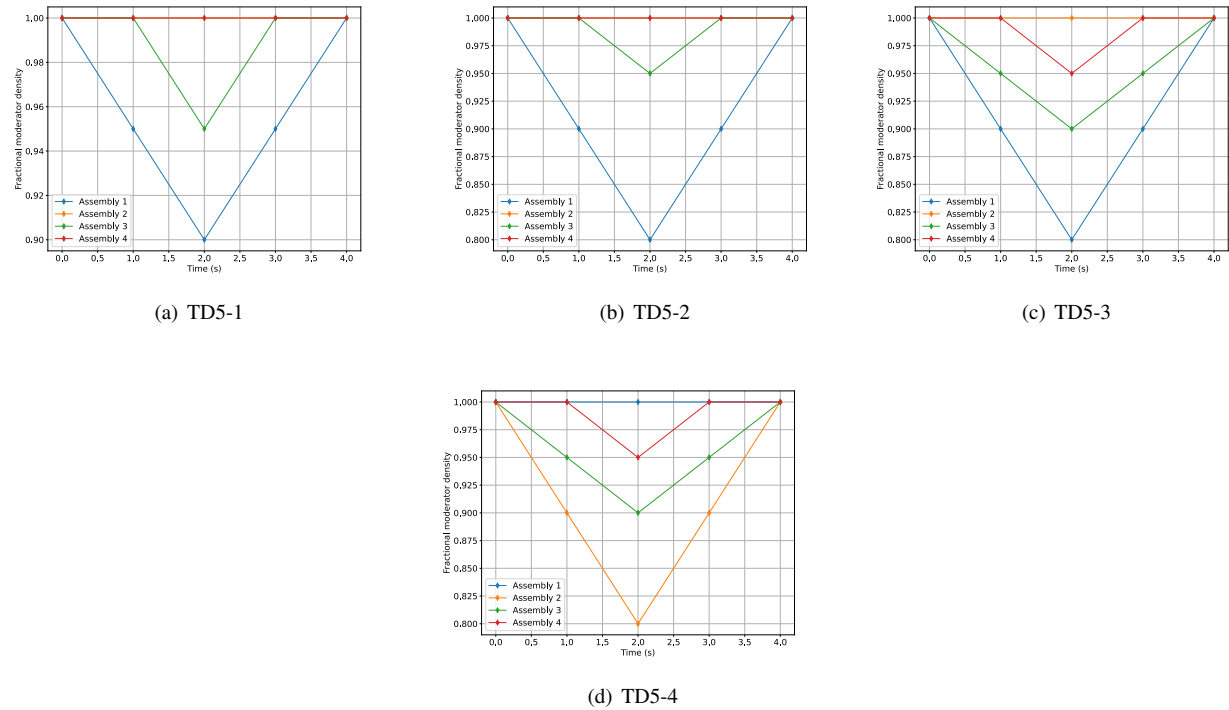


Fig. 12. Fractional moderator density change in TD5 exercise

IV. NUMERICAL RESULTS

the 2D problems and 48 processors for the 3D problems.

Unless otherwise noted, all benchmark problems are simulated with VITAS on a workstation with 16 processors for

Each fuel pin is meshed with three radial rings for the fuel zone, one radial ring for the moderator zone, and eight azimuthal sectors, as determined by a preliminary h - p sensitivity analysis[11]. In total, the mesh is comprised of 32 elements shown in Fig. 2. In the 3D calculation, the axial direction is discretized into 32 layers, and the thickness of each layer is 5.355 cm for TD5 exercise. In TD4 exercise, the axial direction is discretized into 48 layers to better describe the control rod movement. For the spatial expansion within the node, the x - y plane is expanded with continuous FE basis functions of 2nd order, and the axial direction is expanded with orthonormal polynomials of 2nd order. In addition, the interface is approximated with orthonormal polynomials of 2nd order. For the angular expansion, a 25×25 square Legendre-Chebyshev cubature is used to evaluate angular integrals within the node, and the spherical harmonics functions of P_{23} , P_3 and P_3 are implemented on the lateral and axial interfaces, respectively. Table 2 presents a summary of the parameters. To reduce the computational effort, the 2D/1D approach (for 3D problem) and the quasi-reflected interface condition of up to P_3 are applied.

A. Steady-state results

For steady-state calculations, Table 3 compares the eigenvalue results of the 2D and 3D initial eigenvalue problems calculated by different solvers[5, 6]. VITAS results are consistent with those of other solvers. For the 2D case, the difference in eigenvalues between VITAS and MCNP5 is 29 pcm, which is less than the Monte Carlo uncertainty of 0.07%; for the 3D case, the difference between VITAS and PROTEUS-MOC is 25 pcm. The minor deviations indicate that the model is accurate for the initial condition. In addition, the eigenvalues of the forward and adjoint calculations are consistent with a difference of 1 pcm.

Meanwhile, the normalized pin-wise fission rate distributions of 2D and 3D problems are depicted in Fig. 13 and Fig. 14, respectively. The normalization is implemented by scaling the initial total fission rate to unity.

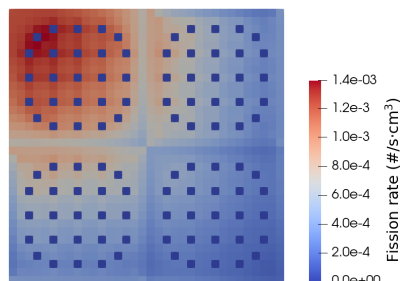


Fig. 13. Pin-wise fission rate distribution at the steady-state of 2D cases

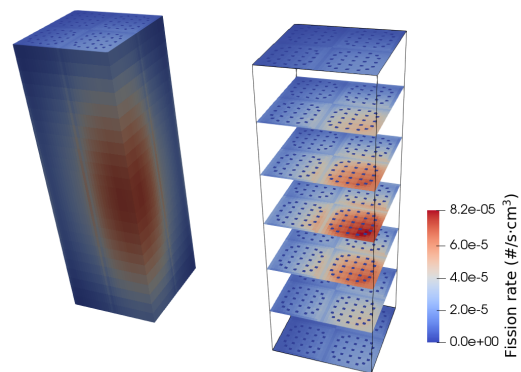


Fig. 14. Pin-wise fission rate distribution at the steady-state of 3D cases

B. Verification of direct-SCM solver

To verify the direct-SCM solver in VITAS, VITAS results are compared with results by MPACT[4] and PANDAS-MOC[6]. MPACT implements a novel Transient Multilevel (TML) approach that involves three levels of calculation: 3D-transport, 3D-Coarse Mesh Finite Difference (CMFD) and EPKE, in order to enhance computational efficiency. The coarse time-step solution of 3D-transport is corrected with fine time-step solutions of CMFD and EPKE. In PANDAS-MOC, the transient solution is solved by coupling the 2D MOC and 1D nodal methods accelerated by the multi-level CMFD methods. Due to the large reactivity insertion, the core power in the TD3-4 problem fluctuates rapidly. Consequently, the TD3-4 problem is chosen as a representative for the time-step size sensitivity analysis.

The fractional core fission rates obtained with time-step sizes ranging from 10 ms to 200 ms are depicted in Fig. 15(a). Fig. 15(b) illustrates the reference solution and the percentage differences between the reference solution and solutions with larger time-step sizes. The reference solution is obtained with a time-step size of 1 ms using the direct-SCM solver. The percentage difference ε is calculated as:

$$\varepsilon(t) = \frac{P(t) - P^*(t)}{P(t_0)} \times 100\% \quad (58)$$

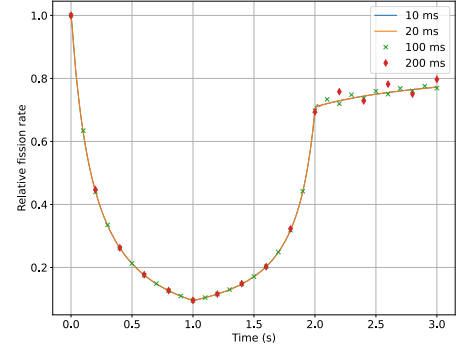
where the superscript $*$ denotes the reference solution. Fig. 15(a) indicates that as the time-step size increases to $\Delta t = 100$ ms or 200 ms, there exists oscillation in the fission rate at the asymptotic stage ($t = 2 \sim 3$ s). Similarly, the oscillation of the percentage difference is demonstrated in Fig. 15(b). The numerical oscillation is attributed to the linear approximation of the amplitude frequency when a large time-step size is utilized. At the asymptotic stage, the control rods are completely withdrawn from the active region, and the fission rate increases gradually due to the delayed neutrons from precursors. Due to the slower growth rate of the fission rate, the numerical oscillation becomes dominant at the asymptotic stage. It also explains that there is no observable oscillation when the fission rate changes rapidly during $t = 0 \sim 2$ s.

TABLE 2. Parameters of VITAS calculation model

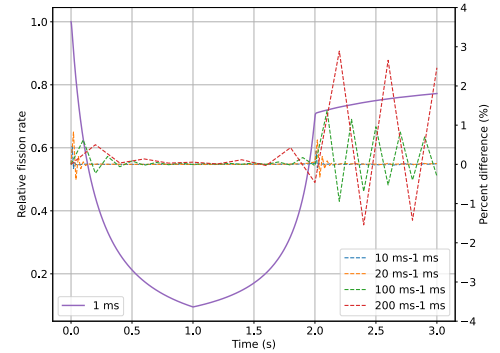
| Model parameters | Value |
|---|--|
| Fuel pin mesh (fuel zone rings/moderator rings/azimuthal sectors) | 3/1/8 |
| Volume spatial expansion order | 2 |
| Surface spatial expansion order | 2 |
| Volume angular integrals | 25×25 Square Legendre-Chebyshev cubature |
| Surface P_N order (lateral interfaces/axial interfaces) | P_{23} - P_3 / P_3 |
| Number of axial meshes in 3D | 48 (TD4), 32 (TD5) |

TABLE 3. Eigenvalue results for steady-states of 2D and 3D C5G7-TD cases

| Code | Method | 2D eigenvalue | 3D eigenvalue |
|-----------------|-----------|---------------|---------------|
| MCNP5 | MC | 1.18646±0.07% | |
| PROTEUS-MOC | 3D MOC | 1.18651 | 1.16469 |
| MPACT | 2D/1D MOC | 1.18666 | 1.16359 |
| NECP-X | 2D/1D MOC | 1.18695 | |
| PANDAS-MOC | 2D/1D MOC | 1.18631 | 1.16512 |
| VITAS (Forward) | VNM | 1.18675 | 1.16494 |
| VITAS (Adjoint) | VNM | 1.18674 | 1.16493 |



(a) Fractional fission rate



(b) Percentage difference

Fig. 15. Fractional fission rate and percentage difference of difference time-step sizes in TD3-4

TABLE 4. Maximum difference and RMS error of different time-step sizes in TD3-4

| Step size (ms) | Max . Diff. (%) | RMS error (%) |
|----------------|-----------------|---------------|
| 10 | 0.463% | 0.035% |
| 20 | 0.826% | 0.099% |
| 100 | 1.370% | 0.499% |
| 200 | 2.889% | 1.288% |

$$\text{RMS} = \sqrt{\frac{\sum_{n=0}^N [P(t_n) - P^*(t_n)]^2}{N}} \quad (59)$$

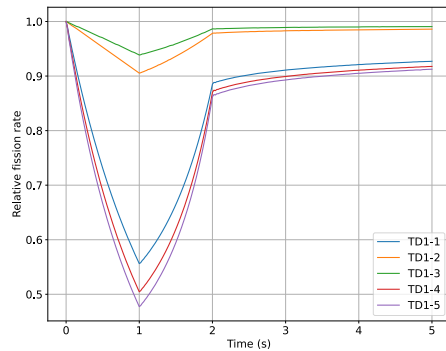
1. 2D results

In this section, results of 2D exercises with ramp-perturbations are discussed, which include TD-1, TD-2 and TD-3. To access the accuracy of the simulation, the results of VITAS are compared to those of MPACT[4] and PANDAS-MOC[6]. Percentage differences are evaluated using MPACT

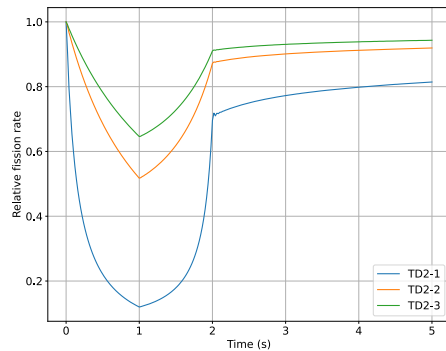
and PANDAS-MOC as references. The time-step sizes employed in MPACT and PANDAS-MOC are 10 ms and 20 ms, respectively. It should also be noted that PANDAS-MOC uses an increased time-step size of 100 ms and 50 ms in the asymptotic stage of TD1/2 and TD3 exercises.

The fractional fission rates of TD1 and TD2 exercises are depicted in Fig. 16. In these problems, continuous changes of fractional fission rates are observed due to the movement of control rods with a constant speed. Despite that fact that the speed of insertion and withdrawal are identical, the increase rate of the fission rate after 1 s is less than the decrease rate before 1 s due to the reduction of the precursor concentration. The fission rate then increases asymptotically to a value

smaller than the initial value. Due to the deeper insertion of control rods in TD2, the fission rate changes more rapidly in TD2. Fig. 17 and Fig. 18 compare the direct-SCM solver's results with those of MPACT and PANDAS-MOC. Comparisons reveal that VITAS with the direct-SCM agrees well with other codes for 2D control rods movement problems. Fig. 19 depicts the fractional fission rate histories of TD3. Due to the similar pattern of perturbations caused by the moderator density change, the fission rate exhibits similar tendencies. As seen in Fig. 20, the direct-SCM solver's results of TD3 are also consistent with those of other codes.



(a) TD1



(b) TD2

Fig. 16. Fractional fission rate of TD1 and TD2 exercises

Table 5 summarized the RMS error and maximum percentage differences in TD1, 2, and 3 exercises. Compared with the rest cases, the solutions of TD2-1 and TD3-4 show greater deviations with maximum percentage differences of 1.0%. It is observed that, as depicted in Fig. 18 and Fig. 20, the maximum differences appear in few time-steps after the introduction of the reactivity. Since the reactivity insertion is substantial and fission rate changes rapidly in TD2-1 and TD3-4, different temporal discretization schemes can lead to larger discrepancies. However, these discrepancies are less than 1.0%, which implies that the direct-SCM solver of VITAS is capable of performing accurate calculation for 2D ramp-perturbation problems.

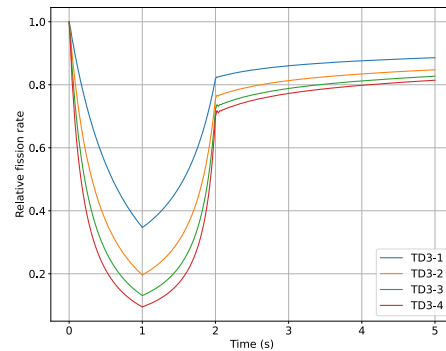


Fig. 19. Fractional fission rate of TD3 exercise

TABLE 5. Maximum difference and RMS error of 2D results

| Problem | MPACT | | PANDAS | |
|---------|---------------|-------------|---------------|-------------|
| | Max. Diff.(%) | RMS Err.(%) | Max. Diff.(%) | RMS Err.(%) |
| 1-1 | -0.13 | 0.08 | 0.14 | 0.06 |
| 1-2 | -0.16 | 0.08 | -0.16 | 0.08 |
| 1-3 | -0.14 | 0.07 | -0.14 | 0.06 |
| 1-4 | -0.17 | 0.07 | 0.17 | 0.06 |
| 1-5 | -0.17 | 0.08 | 0.27 | 0.08 |
| 2-1 | 0.91 | 0.10 | 0.91 | 0.10 |
| 2-2 | -0.21 | 0.11 | -0.23 | 0.15 |
| 2-3 | -0.12 | 0.05 | -0.11 | 0.04 |
| 3-1 | 0.25 | 0.11 | 0.29 | 0.16 |
| 3-2 | 0.45 | 0.11 | 0.56 | 0.16 |
| 3-3 | 0.72 | 0.11 | 0.72 | 0.15 |
| 3-4 | 0.97 | 0.11 | 0.97 | 0.14 |

2. 3D results

In this section, results of 3D TD4 and TD5 exercises are discussed. In TD4 and TD5, VITAS employs time-step sizes of 25 ms and 20 ms, respectively. MPACT and PANDAS-MOC employ time-step sizes of 25 ms and 20 ms, respectively. At the asymptotic stage, the PANDAS-MOC time-step sizes are increased to 100 ms.

The fractional fission rate history of TD4 exercise is depicted in Fig. 21. In TD4-4 and TD4-5 problems, the fission rate is more complicated since multiple control rod banks are inserted and withdrawn simultaneously. Fig. 22 compares VITAS results to those of MPACT and PANDAS-MOC. The MPACT results are in well agreement with the other code results, with VITAS results being the most comparable to the MPACT results. Oscillation in the percentage difference with a certain period can be observed in the stage of control rod movement. It is attributed to the different de-coupling techniques implemented in different codes. As shown in Table 6, the maximum difference between MPACT and VITAS results is -0.97%, whereas the maximum difference between PANDAS-MOC and VITAS results is 1.57%. The discrepancies between these codes in TD4 are caused not just by the

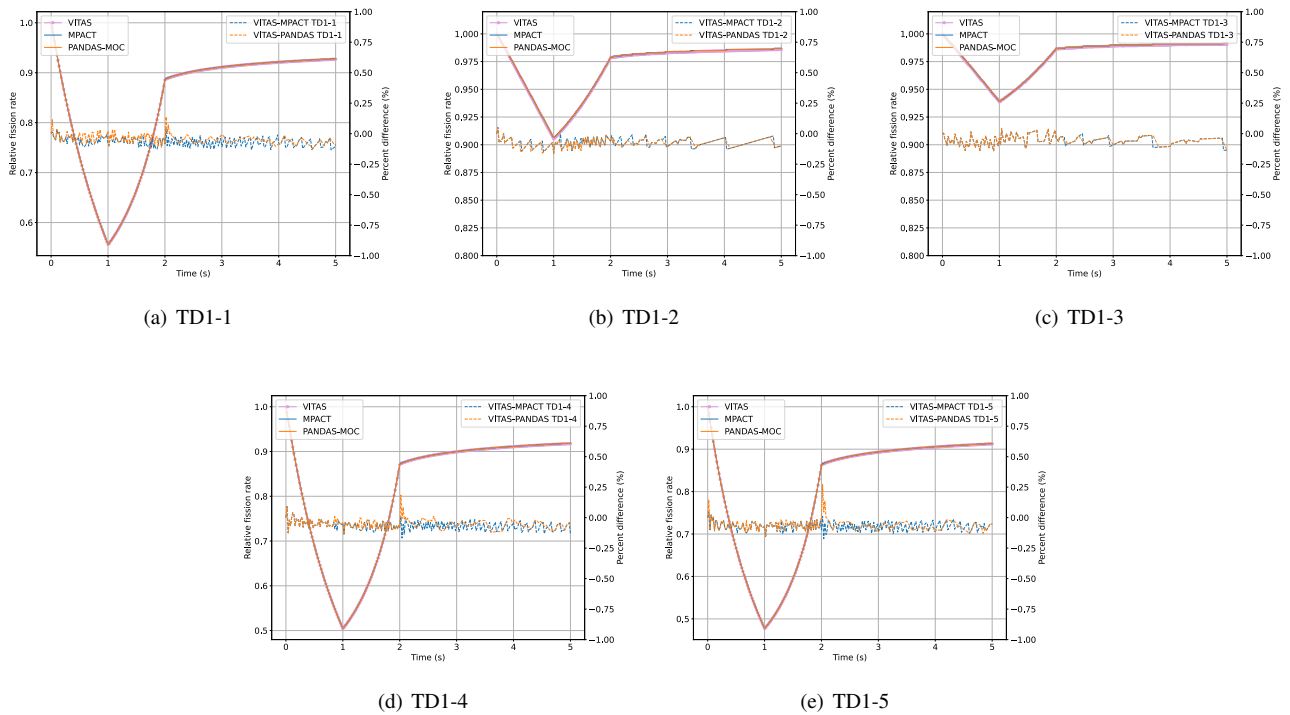


Fig. 17. Fractional fission rate comparisons of VITAS versus MPACT and VITAS versus PANDAS-MOC for TD1 exercise

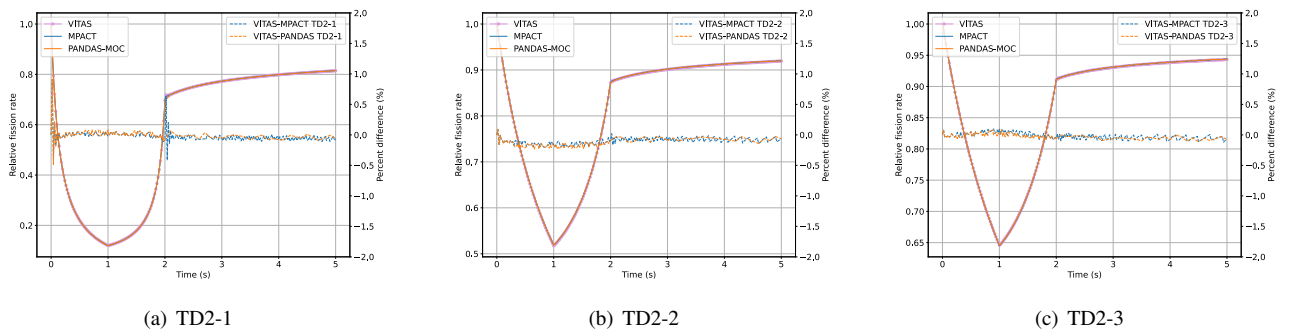


Fig. 18. Fractional fission rate comparisons of VITAS versus MPACT and VITAS versus PANDAS-MOC for TD2 exercise

temporal nor spatial discretization scheme, but also by the decoupling techniques.

TABLE 6. Maximum difference and RMS error of TD4

| Problem | MPACT | | PANDAS | |
|---------|---------------|-------------|---------------|-------------|
| | Max. Diff.(%) | RMS Err.(%) | Max. Diff.(%) | RMS Err.(%) |
| 4-1 | -0.97 | 0.28 | 1.57 | 0.69 |
| 4-2 | -0.77 | 0.28 | 0.68 | 0.28 |
| 4-3 | -0.77 | 0.29 | 0.68 | 0.31 |
| 4-4 | -0.75 | 0.34 | 0.74 | 0.25 |
| 4-5 | -0.97 | 0.39 | 1.57 | 0.62 |

linearly in different fuel assemblies, as shown in Fig. 12. During the first two seconds, the fission rates decrease to the minimal values as the moderator densities decrease. In the subsequent two seconds, the moderator densities are restored to the nominal values, and the fission rate increases gradually. Fig. 24 compares the results of several codes. The comparison demonstrates that the direct-SCM solutions agree well with the MPACT and PANDAS-MOC results. As shown in Table 7, compared with the corresponding MPACT and PANDAS-MOC solutions in TD5-2 problem, the direct-SCM results show maximum differences of 0.87% and 0.85%, respectively.

Fig. 23 presents the evolution of the relative fission rates for the TD5 exercise, in which the moderator density varies

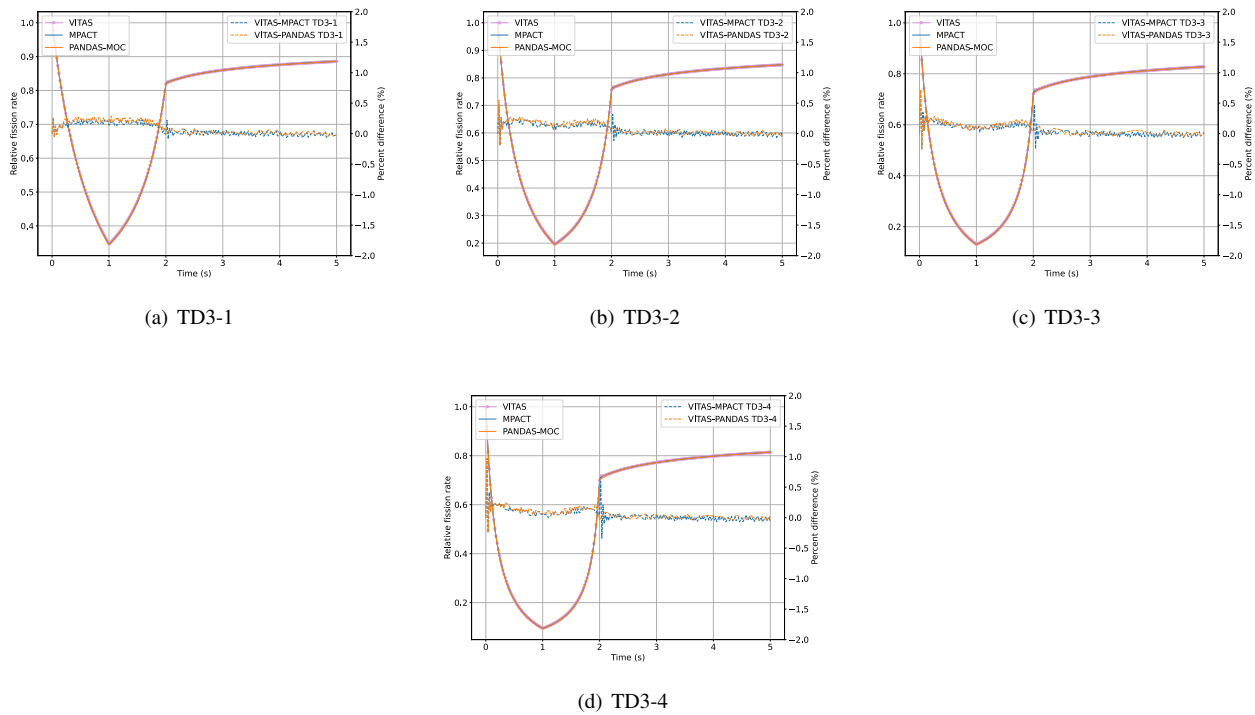


Fig. 20. Fractional fission rate comparisons of VITAS versus MPACT and VITAS versus PANDAS-MOC for TD3 exercise

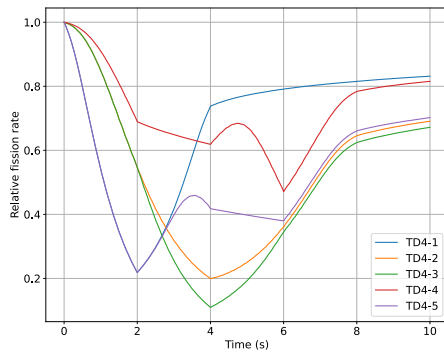


Fig. 21. Fractional fission rate of TD4 exercise

TABLE 7. Maximum difference and RMS error of TD5

| Problem | MPACT | MPACT | PANDAS | PANDAS |
|---------|---------------|-------------|---------------|-------------|
| | Max. Diff.(%) | RMS Err.(%) | Max. Diff.(%) | RMS Err.(%) |
| 5-1 | 0.69 | 0.43 | 0.74 | 0.52 |
| 5-2 | 0.87 | 0.45 | 0.85 | 0.54 |
| 5-3 | 0.85 | 0.38 | 0.78 | 0.47 |
| 5-4 | 0.33 | 0.10 | 0.34 | 0.12 |

3. Step-perturbation results

The TD0 results of VITAS and MPACT are compared in order to validate the direct-SCM solver for step-perturbation problems. Typically, the step-perturbation problem demands finer time-steps to capture the rapid change induced by the step reactivity[7]. For a PCQM solver, a time-step is further discretized into several micro time-steps for EPKE solution. The PCQM solver can therefore simulate the step reactivity with a rather large time-step size without a significant loss of accuracy. However, the direct transient solver requires a finer time-step size. To compare the solutions of the direct-SCM solver with those of MPACT in TD0 exercise, variable time-steps are employed in VITAS.

In the TD0 exercise, the reactivity is introduced abruptly at $t = 0, 1, 2$ s, while the cross-sections stay constant for the remaining transient activity. Consequently, a smaller time-step size can be employed immediately after the step reactivity change; otherwise, a larger time-step size is used. The time-step size employed in MPACT is 10 ms. Fig. 25 illustrates the variable time-step size employed in VITAS, which is 1 ms during the first 20 ms following a step reactivity change, and 20 ms for the remainder of the transient process.

The fractional core fission rates of TD0 exercises are shown in Fig. 26. The fission rates decrease at 0 s and 1 s as the result of the abrupt insertion of control rods, then increase promptly at 2 s with the withdrawal of control rods. After 2 s, all control rods are completely out of the active region, and the fission rates hereby increase asymptotically to a value

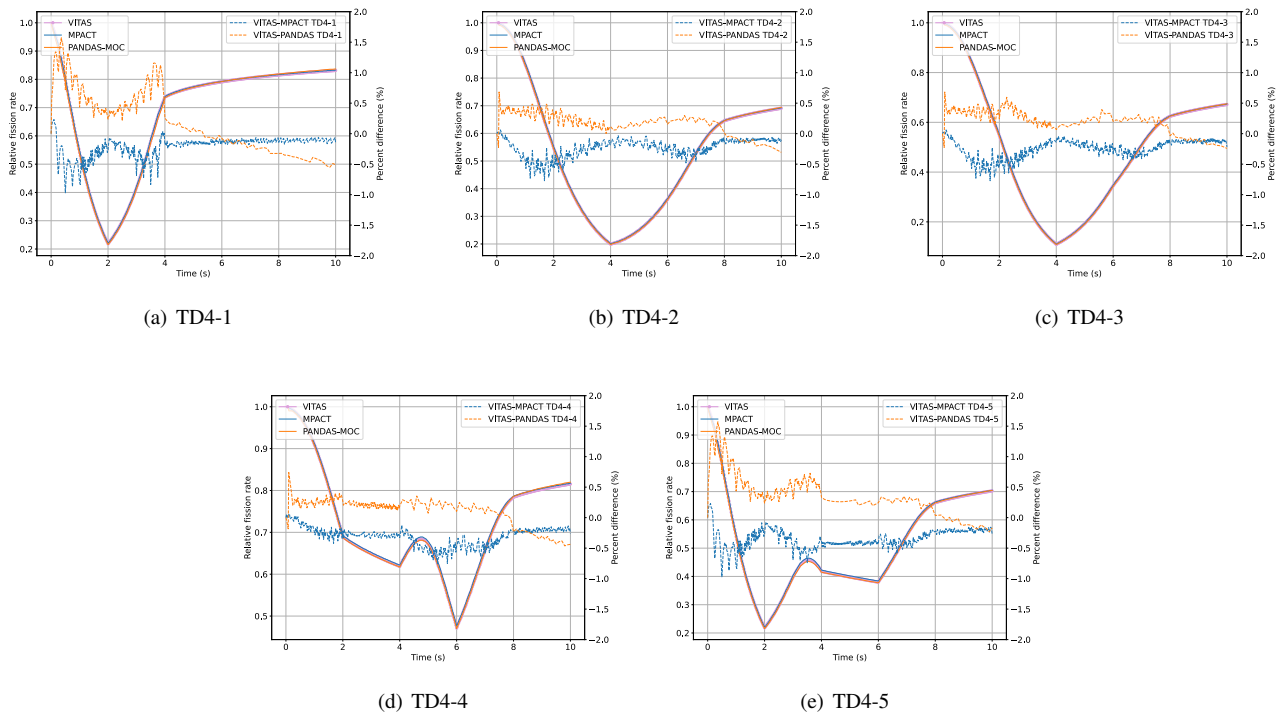


Fig. 22. Fractional fission rate comparisons of VITAS versus MPACT and VITAS versus PANDAS-MOC for TD4 exercise

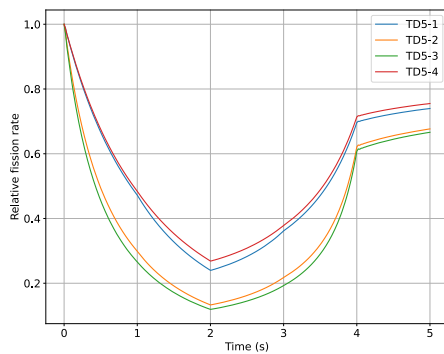


Fig. 23. Fractional fission rate of TD5 exercise

TABLE 8. Maximum difference and RMS error of TD0

| Problem | MPACT | MPACT |
|---------|---------------|-------------|
| | Max. Diff.(%) | RMS Err.(%) |
| 0-1 | -0.12 | 0.05 |
| 0-2 | -0.20 | 0.11 |
| 0-3 | -0.10 | 0.05 |
| 0-4 | -0.11 | 0.05 |
| 0-5 | -0.11 | 0.05 |

C. Performance of PCQ-SCM solver

In the following section, the PCQ-SCM solver is tested against the direct-SCM solver using three problems: TD0-5, TD3-4, and TD5-1. The numerical accuracy and the computational cost are applied as metrics for evaluating the performance of the method.

Fig. 28 shows that the reactivity evaluated by VITAS is consistent with MPACT results. Fig. 29 compares the results by direct-SCM and PCQ-SCM solvers for the TD0-5 problem. The solution of direct-SCM solver is obtained with a constant time-step size of 1 ms, while the PCQ-SCM calculations employ variable time-step sizes. To capture the step-reactivity, a step-size of 1 ms is employed in the first 1 ms following a step reactivity change, whereas 100 or 200 ms for the remaining. As shown in Fig. 29, the PCQ-SCM solutions are consistent with those of the direct-SCM solver, with the exception of the first 1 ms following the step reactivity change. As shown in Table 9, the percentage differences are

smaller than the initial value. Fig. 27 compares VITAS and MPACT solutions, while Table 27 summarizes the error. The maximum difference of all step-perturbation problems is approximately 0.21% in TD0-2 problem, while the differences in other problems are within 0.12%. They demonstrate that the solutions of VITAS and MPACT are highly consistent, indicating that the direct-SCM solver is capable of generating accurate solutions for step-perturbation problems.

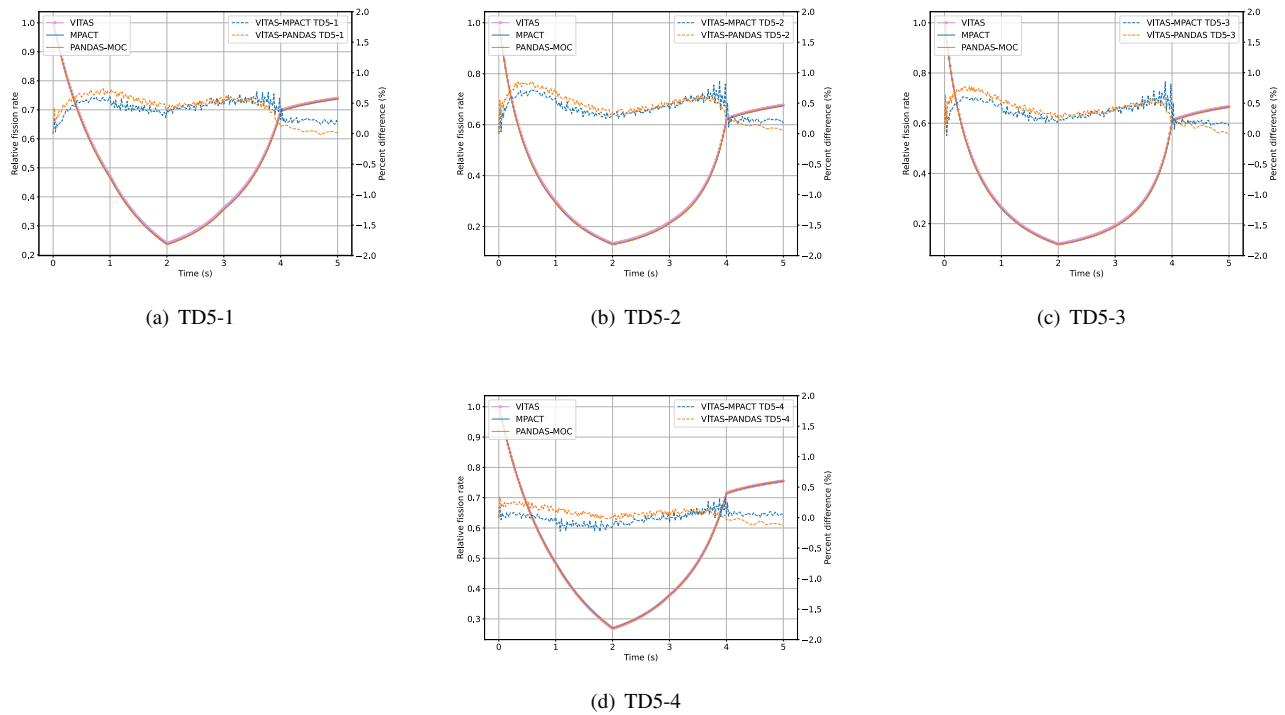


Fig. 24. Fractional fission rate comparisons of VITAS versus MPACT and VITAS versus PANDAS-MOC for TD5 exercise

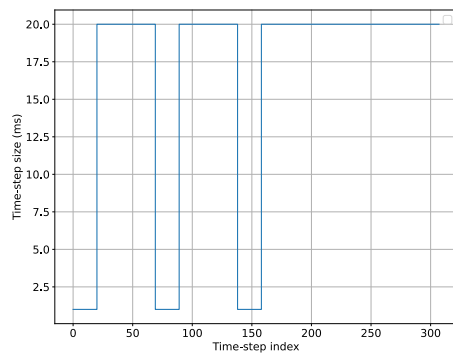


Fig. 25. Variable time-step sizes of VITAS for TD0 exercise

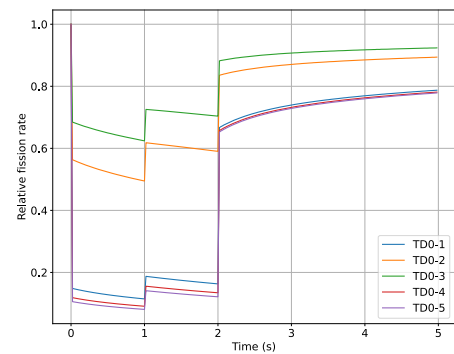


Fig. 26. Fractional fission rate of TD0 exercise

within 0.08% in both time-step sizes. Note that when calculating the RMS error and maximum percentage difference displayed in Table 9, the results at the first 1 ms following the reactivity change are not included. The significant discrepancies following the reactivity change cause by the errors in the direct-SCM solution. The step size of 1 ms in the direct solver is insufficient to trace the step response of the fission rate; however, for the PCQ-SCM solver, the first 1 ms is further subdivided into 100 micro-steps. The micro-step size of 0.01 ms is capable of simulating the step response accurately.

In addition, Table 9 displays the computing time for different solvers. In comparison to the direct solution, the number

of TEVPs in the PCQ-SCM solution with a step size of 100 ms decreases from 5000 to 53, and the computing time decreases from 14 minutes to 7 minutes. The incommensurate decrease of computing time can be attributed to the fact that the computing time is dominated by response matrix formation in 2D calculations. In the transient solvers of VITAS, the response matrices are only updated when the cross-sections are altered. In the TD0-5 problem, increasing time-step size to 100 ms accelerates the iteration for flux solving but not the response matrix formation. Therefore, the computational cost reduction brought by the PCQ-SCM solver is insignificant in TD0 exercises.

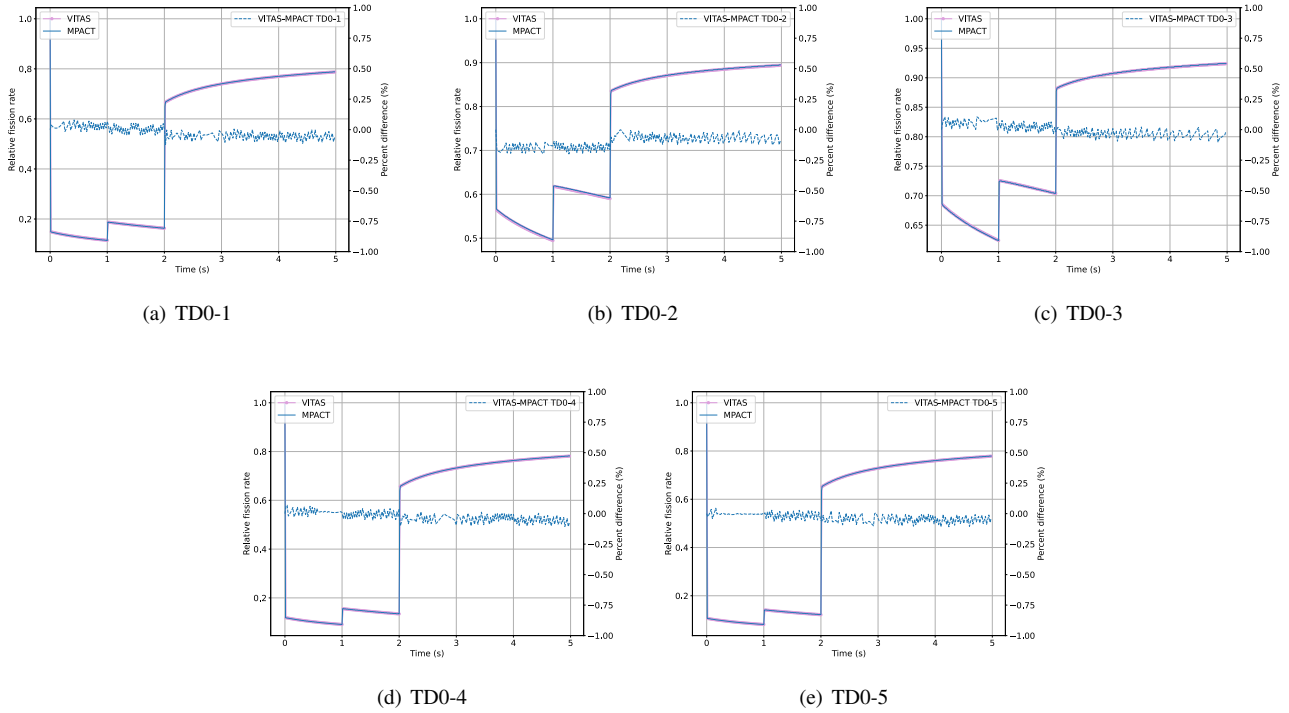


Fig. 27. Fractional fission rate comparisons of VITAS versus MPACT and VITAS versus PANDAS-MOC for TD0 exercise

TABLE 9. Performance comparison of PCQ-SCM for TD0-5 problem (16 processors)

| Method | Δt (ms) | Number of TEVPS | Max. Diff. (%) | RMS Err. (%) | Computing time (min) | Speedup factor |
|--------|-----------------|-----------------|----------------|--------------|----------------------|----------------|
| Direct | 1 | 5000 | N/A | N/A | 14 | N/A |
| PCQ | 100 | 53 | 0.08 | 0.04 | 7 | 2.0 |
| PCQ | 200 | 28 | 0.08 | 0.04 | 6 | 2.4 |

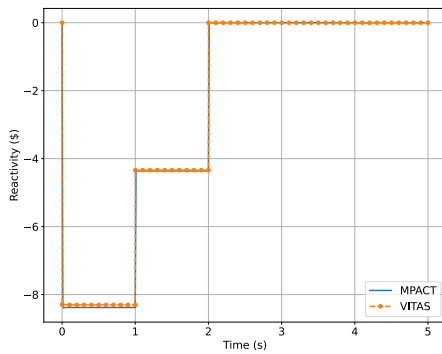
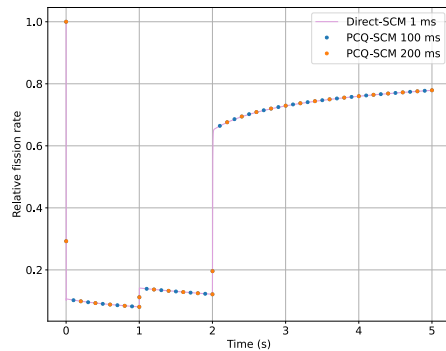


Fig. 28. Comparison of reactivity history for TD0-5 problem

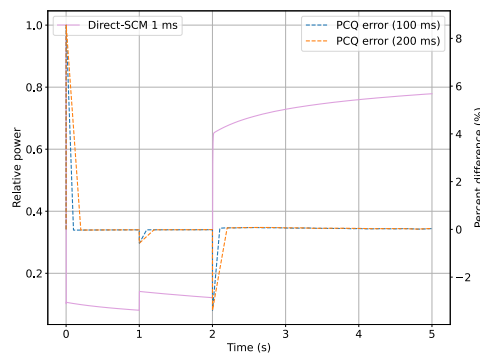
Fig. 30 illustrates the reactivity history of TD3-4 generated by VITAS and MPACT. Although the cross-sections vary linearly in this problem, the reactivity curve versus time shows non-linear. This behavior can be attributed to the spatial ef-

fects caused by the variation of the flux shape. Fig. 31 compares the solutions of direct-SCM and PCQ-SCM solver for the TD3-4 problem. The solutions of direct-SCM solver are obtained with fixed time-step sizes of 1 and 100 ms, and the PCQ-SCM calculations are performed with time-step sizes of 100, 500 and 1000 ms, respectively. Fig. 31(b) shows that as the time-step size of the PCQ-SCM decreases, the PCQ-SCM solution gradually converges to the direct solution. The maximum percentage difference in the solution with a step size of 100 ms is -0.23% as shown in Table 10. It is less than the direct solution with 10 ms shown in Table 4. Additionally, Fig. 31(b) also indicates that in the direct solution with 100 ms, there are significant fluctuations at the asymptotic stage, which leads the maximum difference greater than 1.0%. It indicates that the PCQ-SCM solver can accurately predict the fission rate and eliminate the numerical fluctuations with a large time-step size.

In the meantime, the number of TEVP calculations for the PCQ-SCM calculation with a 100 ms step size is decreased from 10000 to 100, where the linear speedup is 100, and the computing time is reduced by a speedup factor of 78.9. The speedup of TEVP calculations is not proportional to the



(a) Fractional fission rate



(b) Percentage difference

Fig. 29. Comparison of direct-SCM and PCQ-SCM solutions for TD0-5 problem

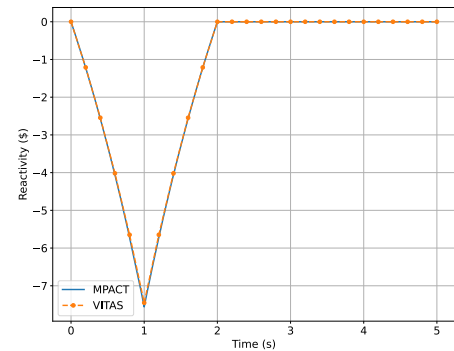
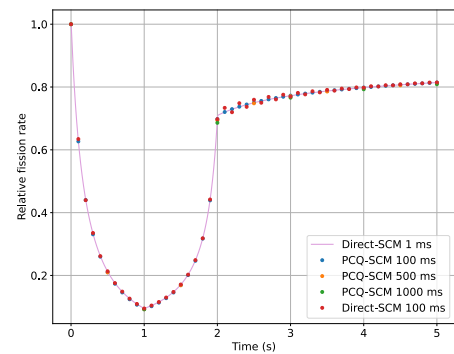
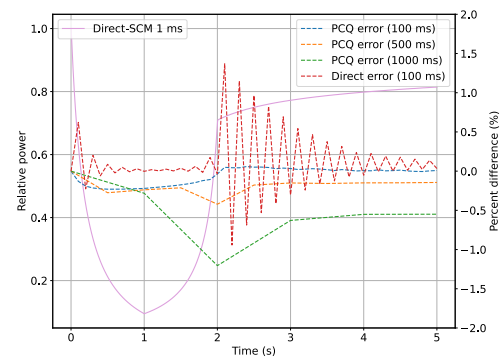


Fig. 30. Comparison of reactivity history for TD3-4 problem



(a) Fractional fission rate



(b) Percentage difference

Fig. 31. Comparison of direct-SCM and PCQ-SCM solutions for TD3-4 problem

speedup of the total computing time. It is because that a larger time-step size makes it more difficult for amplitude frequency, fission source and flux more difficult to converge in the $k - \omega$ iteration. However, the speedup of the overall computing time is close to the linear speedup of TEVP calculations. It implies that the PCQ-SCM solver can reduce the computing time efficiently without a significant loss of the numerical accuracy in the TD3-4 problem.

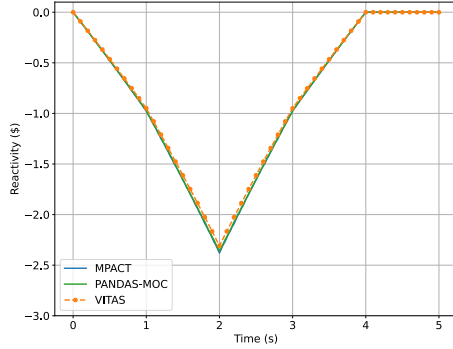
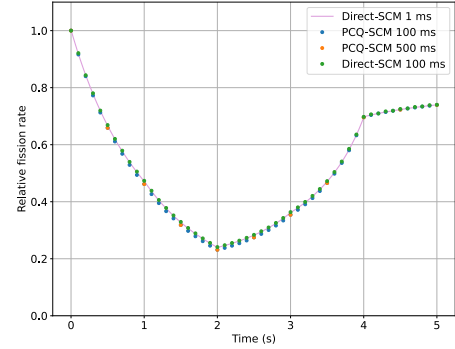
Fig. 32 shows the reactivity history of TD5-1 as evaluated by VITAS, MPACT and PANDAS-MOC. Note that the reactivity displayed in Fig. 32(a) is defined as ρ/β with the unit of \$, whereas it is defined as ρ with the unit of pcm in Fig. 32(b). Fig. 32(a) reveals that compared with the reactivity of MPACT and PANDAS-MOC, VITAS predicts an underestimated ρ/β . However, in Fig. 32(b), the reactivity ρ evaluated by VITAS is consistent with that of PANDAS-MOC. Consequently, the deviations in Fig. 32(a) can be attributed to the discrepancies of the effective delayed neutron fractions $\bar{\beta}$ computed by different codes.

Fig. 33 compares the results of direct-SCM and PCQ-SCM solvers for the TD5-1 problem. The direct solutions are obtained with time-step sizes of 1 and 100 ms. The macro time-step sizes used in the PCQ-SCM calculation are 100

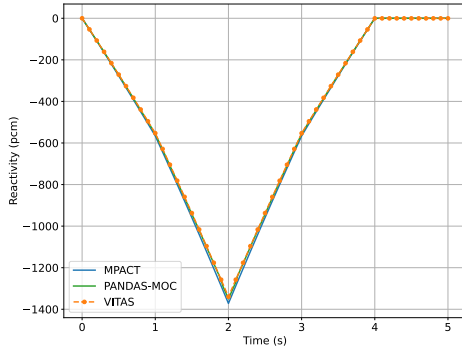
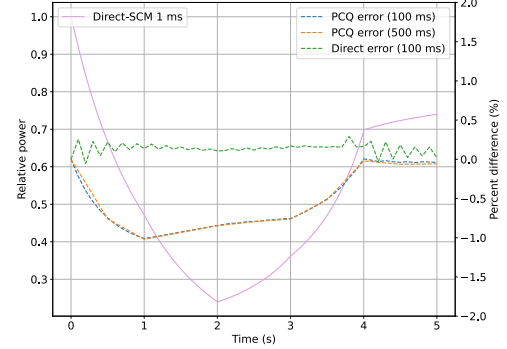
and 500 ms. As shown in Fig. 33, during the first four seconds, the PCQ-SCM calculations provide an underestimated fission rate with respect to the direct-solution. When the cross-sections revert to the nominal value at the asymptotic stage, however, the fission rate values get closer to the reference solution. The discrepancies are shown in Table 11.

TABLE 10. Performance comparison of PCQ-SCM for TD3-4 problem (8 processors)

| Method | Δt (ms) | Number of TEVPS | Max. Diff. (%) | RMS Err. (%) | Computing time (min) | Speedup factor |
|--------|-----------------|-----------------|----------------|--------------|----------------------|----------------|
| Direct | 1 | 10000 | N/A | N/A | 6573 | N/A |
| PCQ | 100 | 100 | -0.23 | 0.12 | 83 | 78.9 |
| PCQ | 500 | 20 | -0.42 | 0.21 | 16 | 405.0 |
| PCQ | 1000 | 10 | -1.21 | 0.65 | 11 | 598.6 |

(a) Reactivity ρ/β 

(a) Fractional fission rate

(b) Reactivity ρ 

(b) Percentage difference

Fig. 32. Comparison of reactivity history for TD5-1 problem

Fig. 33. Comparison of direct-SCM and PCQ-SCM solutions for TD5-1 problem

The maximum difference between the direct solution and the PCQ-SCM solution with 500 ms step size is -1.01%, and the RMS error is 0.66%. When the macro time-step size is refined to 100 ms, the solution and error show no significant change. Additionally, as shown in Fig. 33, compared with PCQ solutions, the direct solution with 100 ms shows smaller differences of less than 0.5%. The deviations between the direct- and PCQ-SCM solutions can be attributed to the inconsistent formulation of the kinetics parameters in VITAS transient models[5].

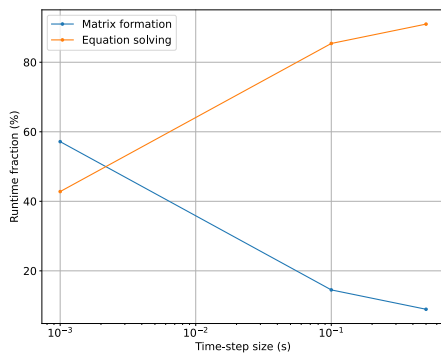
Meanwhile, Table 11 further summarizes the speedup of PCQ-SCM solutions. It shows that the speedup factors in TD5-1 problem are significantly lower than those for TD3-4 problem. The deviation in speedup is due to the different

fractions of computing time in 2D and 3D problems. In VITAS, 99% of the overall runtime is consumed by obtaining response matrices and solving transport equation. Therefore, the following runtime analysis will focus on matrix formation and equation solving. Fig. 34(a) shows the fractional runtime of matrix formation and equation solving for TD5-1 problem. When the time-step size is 1 ms, matrix formation and equation solving account for 57.16% and 42.80% of the runtime, respectively. However, when using a time-step size of 100 ms or 500 ms for PCQ-SCM solutions, equation solving is becoming dominant in the total runtime. Fig. 34(b) depicts the speedup of matrix formation, equation solving, and total calculation. The speedup of the matrix formation is close to the linear speedup, whereas the speedup of the equation

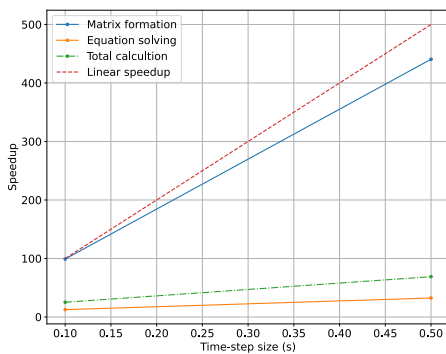
TABLE 11. Performance comparison of PCQ-SCM for TD5-1 problem (48 processors)

| Method | Δt (ms) | Number of TEVPS | Max. Diff. (%) | RMS Err. (%) | Computing time (min) | Speedup factor |
|--------|-----------------|-----------------|----------------|--------------|----------------------|----------------|
| Direct | 1 | 500 | N/A | N/A | 6820 | N/A |
| PCQ | 100 | 50 | -1.00 | 0.66 | 271 | 25.2 |
| PCQ | 500 | 10 | -1.01 | 0.65 | 99 | 68.9 |

solving is significantly below the linear speedup. As noted previously, the fission source and flux require more iterations to get converged when time-step size is increased. Therefore, the equation solving speedup is not proportional to the linear speedup. As the time-step size increases, the runtime time is dominated by the equation solving, and the speedup of the total calculation is primarily determined by the speedup of the equation solving.



(a) Runtime fraction



(b) Speedup

Fig. 34. Runtime analysis of the PCQ-SCM solutions for TD5-1 problem

V. CONCLUSION

This work discusses the direct-SCM and PCQ-SCM transient models of the VITAS code, as well as the verification of these models using the C5G7-TD benchmark. In the formu-

lation of the direct-SCM, the SCM transforms the transient transport equation into a TEVP, and then the solution of the TEVP is solved by the heterogeneous VNM. In addition, the PCQ-SCM is proposed and developed to reduce the computational cost. The predicted neutron flux in the PCQ-SCM is obtained by solving the TVEP, and is then corrected by the EPKE solution. For the formulation of the EPKE, the methods for computing the reactivity and adjoint flux within the heterogeneous VNM are discussed. Due to the second-order even-parity form of the transport equation in the VNM, the adjoint equation can be easily solved by creating the adjoint source without generating additional response matrices. For the calculation of reactivity, the exact reactivity is determined using the dynamic eigenvalue acquired from the TEVP, without the need to reconstruct the angular flux or apply perturbation theory.

To verify the direct-SCM solver, four C5G7-TD 2D benchmark exercises and two 3D benchmark exercises are examined. The direct-SCM solver's transient results are in good agreement with those previously published by MPACT and PANDAS-MOC. In 2D problems, the percentage difference relative to other reference solutions is within 0.97%, while in 3D problems, the difference is within 0.97% and 1.57% compared with MPACT and PANDAS-MOC results, respectively. It demonstrates the correctness of the direct-SCM implemented in VITAS. In addition, the performance of the PCQ-SCM solver is compared to the performance of the direct-SCM solution on TD0-5, TD3-4, and TD5-1 problems. Due to the response matrix update strategy implemented in VITAS, the PCQ-SCM can minimize the computing time for step-perturbation problem TD0-5 by approximately twofold as it decreases the number of iterations with larger time steps. For ramp-perturbation problems, PCQ-SCM with larger time-steps is capable of drastically lowering the number of response matrices and power iterations. The computing time for various problems, such as TD3-4, can be saved by one to two magnitude without sacrificing accuracy. Meanwhile, the analysis to the computing time reveals that the speedup efficiency of PCQ-SCM is determined by the runtime fractions of the matrix formation and equation solving. In 2D ramp-perturbation problem, where the matrix formation typically dominates the runtime, the PCQ-SCM has a high speedup efficiency; whereas in 3D problems, it exhibits a lower speedup efficiency since the equation solving is dominant in the runtime.

Future efforts will focus on improving the parallel efficiency of the code so that it can be deployed on clusters to solve more complex problems. Moreover, the high-fidelity transient multi-physics coupling of the neutron transport method with thermal-hydraulic simulations, and the un-

certainty analysis[33] to the transient multi-physics calculation will be investigated.

DECLARATION OF COMPETING INTEREST

The authors declare that they have no known competing financial interests or personal relationships that could have

appeared to influence the work reported in this paper.

ACKNOWLEDGEMENTS

This research is supported by the National Natural Science Foundation of China [12175138, U20B2011], Young Talent Project of China National Nuclear Corporation. We would like to thank Professor Yunlin Xu of Purdue University for providing the detailed C5G7-TD benchmark results data of PANDAS-MOC.

- [1] G. Zhong, K. Xu, Y. Lu, et al., Study on application of DAG-OPENMC in fusion neutronics analysis. *Nuclear Techniques*. **45(5)**, 76-84(2022). doi: [10.11889/j.0253-3219.2022.hjs.45.050602](https://doi.org/10.11889/j.0253-3219.2022.hjs.45.050602)
- [2] Z. Zeng, S. Chen, Y. Zhang, et al., Neutronics experiments of dual functional lithium-lead blanket based on D-T fusion neutron source. *Nuclear Techniques*. **45(4)**, 040601-040601(2022). doi: [10.11889/j.0253-3219.2022.hjs.45.040601](https://doi.org/10.11889/j.0253-3219.2022.hjs.45.040601)
- [3] X. Du, Y. Wang, Y. Zheng, et al., The steady-state neutronic analysis and transient simulation of ADANES reactor design based on deterministic method. *Nuclear Techniques*. **45(10)**, 100601(2022). doi: [10.11889/j.0253-3219.2022.hjs.45.100601](https://doi.org/10.11889/j.0253-3219.2022.hjs.45.100601)
- [4] Q. Shen, Y. Wang, D. Jabaay, et al., Transient analysis of C5G7-TD benchmark with MPACT. *Ann. Nucl. Energy*. **125**, 107-120(2019). doi: [10.1016/j.anucene.2018.10.049](https://doi.org/10.1016/j.anucene.2018.10.049)
- [5] A. Hsieh, G. Zhang, W. S. Yang, Consistent Transport Transient Solvers of the High-Fidelity Transport Code PROTEUS-MOC. *Nucl. Sci. Eng.* **194(7)**, 508-540(2020). doi: [10.1080/00295639.2020.1746619](https://doi.org/10.1080/00295639.2020.1746619)
- [6] S. Tao, Y. Xu, Neutron transport analysis of C5G7-TD benchmark with PANDAS-MOC. *Ann. Nucl. Energy*. **169**, 108966(2022). doi: [10.1016/j.anucene.2022.108966](https://doi.org/10.1016/j.anucene.2022.108966)
- [7] B. Wang, Z. Liu, J. Chen, et al., A modified predictor-corrector quasi-static method in NECP-X for reactor transient analysis based on the 2D/1D transport method. *Prog. Nucl. Energy*. **108**, 122-135(2018). doi: [10.1016/j.pnucene.2018.05.014](https://doi.org/10.1016/j.pnucene.2018.05.014)
- [8] Z. Shen, Q. Sun, D. He, et al., Comparison and verification of NECP-X and OpenMC using high-fidelity BEAVRS benchmark models. *Nuclear Techniques*. **45(01)**, 73-81(2022). doi: [10.11889/j.0253-3219.2022.hjs.45.010602](https://doi.org/10.11889/j.0253-3219.2022.hjs.45.010602)
- [9] Y. Wang, S. Schunert, J. Ortensi, et al., Rattlesnake: A MOOSE-Based Multiphysics Multischeme Radiation Transport Application. *Nuclear Technology*. **207(7)**, 1047-1072(2021). doi: [10.1080/00295450.2020.1843348](https://doi.org/10.1080/00295450.2020.1843348)
- [10] T. Zhang, Z. Li, Variational nodal methods for neutron transport: 40 years in review. *Nucl. Eng. Technol.* **54(9)**, 3181-3204(2022). doi: [10.1016/j.net.2022.04.012](https://doi.org/10.1016/j.net.2022.04.012)
- [11] T. Zhang, Y. Wang, E. E. Lewis, et al., A Three-Dimensional Variational Nodal Method for Pin-Resolved Neutron Transport Analysis of Pressurized Water Reactors. *Nucl. Sci. Eng.* **188(2)**, 160-174(2017). doi: [10.1080/00295639.2017.1350002](https://doi.org/10.1080/00295639.2017.1350002)
- [12] T. Zhang, E. E. Lewis, M. A. Smith, et al., A Variational Nodal Approach to 2D/1D Pin Resolved Neutron Transport for Pressurized Water Reactors. *Nucl. Sci. Eng.* **186(2)**, 120-133(2017). doi: [10.1080/00295639.2016.1273023](https://doi.org/10.1080/00295639.2016.1273023)
- [13] M. A. Smith, E. E. Lewis, E. R. Shemon, DIF3D-VARIANT 11.0: A Decade of Updates. (2017). doi: [10.2172/1127298](https://doi.org/10.2172/1127298)
- [14] Y. Wang, H. Wu, Y. Li, Comparison of two three-dimensional heterogeneous variational nodal methods for PWR control rod cusping effect and pin-by-pin calculation. *Prog. Nucl. Energy*. **101**, 370-380(2017). doi: [10.1016/j.pnucene.2017.06.002](https://doi.org/10.1016/j.pnucene.2017.06.002)
- [15] T. Zhang, W. Xiao, H. Yin, et al., VITAS: A multi-purpose simulation code for the solution of neutron transport problems based on variational nodal methods. *Ann. Nucl. Energy*. **178**, 109335(2022). doi: [10.1016/j.anucene.2022.109335](https://doi.org/10.1016/j.anucene.2022.109335)
- [16] F. He, X. Cai, W. Guo, et al., The transient analysis of molten salt reactor reactivity insertion based on RELAP5/FLUENT coupled program. *Nuclear Techniques*. **44(3)**, 030601(2021). doi: [10.11889/j.0253-3219.2021.hjs.44.030601](https://doi.org/10.11889/j.0253-3219.2021.hjs.44.030601)
- [17] S. Dulla, E. H. Mund, P. Ravetto, The quasi-static method revisited. *Prog. Nucl. Energy*. **50(8)**, 908-920(2008). doi: [10.1016/j.pnucene.2008.04.009](https://doi.org/10.1016/j.pnucene.2008.04.009)
- [18] D. Caron, S. Dulla, P. Ravetto, New aspects in the implementation of the quasi-static method for the solution of neutron diffusion problems in the framework of a nodal method. *Ann. Nucl. Energy*. **87**, 34-48(2016). doi: [10.1016/j.anucene.2015.02.035](https://doi.org/10.1016/j.anucene.2015.02.035)
- [19] Y.-A. Chao, A. Attard, A Resolution of the Stiffness Problem of Reactor Kinetics. *Nucl. Sci. Eng.* **90(1)**, 40-46(1985). doi: [10.13182/NSE85-A17429](https://doi.org/10.13182/NSE85-A17429)
- [20] S. Aoki, T. Suemura, J. Ogawa, et al., The Verification of 3 Dimensional Nodal Kinetics Code ANCK Using Transient Benchmark Problems. *J. Nucl. Sci. Technol.* **44(6)**, 862-868(2007). doi: [10.1080/18811248.2007.9711323](https://doi.org/10.1080/18811248.2007.9711323)
- [21] B. W. Park, H. G. Joo, Improved stiffness confinement method within the coarse mesh finite difference framework for efficient spatial kinetics calculation. *Ann. Nucl. Energy*. **76**, 200-208(2015). doi: [10.1016/j.anucene.2014.09.029](https://doi.org/10.1016/j.anucene.2014.09.029)
- [22] C. Tang, Application of Stiffness Confinement Method in Transient Transport Calculation. *J. Nucl. Eng. Radiat. Sc.* **6(1)**(2019). doi: [10.1115/1.4044749](https://doi.org/10.1115/1.4044749)
- [23] W. Xiao, Q. Sun, X. Liu, et al., Application of stiffness confinement method within variational nodal method for solving time-dependent neutron transport equation. *Comput. Phys. Commun.* **279**, 108450(2022). doi: [10.1016/j.cpc.2022.108450](https://doi.org/10.1016/j.cpc.2022.108450)
- [24] E.E. Lewis, W.F. Miller, *Computational Methods of Neutron Transport*. (Wiley-Interscience, 1993)
- [25] K. O. Ott, D. A. Meneley, Accuracy of the Quasistatic Treatment of Spatial Reactor Kinetics. *Nucl. Sci. Eng.* **36(3)**, 402-411(1969). doi: [10.13182/NSE36-402](https://doi.org/10.13182/NSE36-402)
- [26] M. Kheradmand Saadi, A. Abbaspour, Effective point kinetic parameters calculation in Tehran research reactor using deterministic and probabilistic methods. *Nucl. Sci. Tech.* **28(12)**, 171(2017). doi: [10.1007/s41365-017-0323-7](https://doi.org/10.1007/s41365-017-0323-7)

- [27] K. F. Laurin-Kovitz, E. E. Lewis, Variational Nodal Transport Perturbation Theory. Nucl. Sci. Eng. **123**(3), 369-380(1996). doi: [10.13182/NSE96-A24200](https://doi.org/10.13182/NSE96-A24200)
- [28] A. Zhu, Y. Xu, T. Downar, A Multilevel Quasi-Static Kinetics Method for Pin-Resolved Transport Transient Reactor Analysis. Nucl. Sci. Eng. **182**(4), 435-451(2016).doi: [10.13182/NSE15-39](https://doi.org/10.13182/NSE15-39)
- [29] F. Alcaro, S. Dulla, P. Ravetto, Implementation of the quasi-static method for neutron transport. International Conference on Mathematics and Computational Methods Applied to Nuclear Science and Engineering (M&C 2011), Rio de Janeiro, RJ, Brazil, May 8-12, 2011.
- [30] W. M. Stacey, *Nuclear reactor physics*, 2nd edn. (WILEY-VCH, Weinheim, 2007), pp. 603-604.
- [31] J. Hou, K. Ivanov, V. Boyarinov, et al., C5G7-TD Benchmark for Time-Dependent Heterogeneous Neutron Transport Calculations. International Conference on Mathematics and Computational Methods Applied to Nuclear Science and Engineering (M&C 2011), Jeju, Korea, 2017.
- [32] J. Hou, K. N. Ivanov, V. F. Boyarinov, et al., OECD/NEA benchmark for time-dependent neutron transport calculations without spatial homogenization. Nucl. Eng. Des. **317**, 177-189(2017). doi: [10.1016/j.nucengdes.2017.02.008](https://doi.org/10.1016/j.nucengdes.2017.02.008)
- [33] C. Hao, J. Ma, X. Zhou, et al., Development, verification and application of the uncertainty analysis platform CUSA. Ocean Engineering. **261**, 112160(2022). doi: [10.1016/j.oceaneng.2022.112160](https://doi.org/10.1016/j.oceaneng.2022.112160)